NUWC-NPT Technical Report 10,568
15 April 1996

Gaussian Ray Bundles for Modeling High-Frequency Propagation Loss Under Shallow-Water Conditions

Henry Weinberg
Environmental and Tactical Support Systems Department

Ruth E. Keenan
Scientific Applications International Corporation

Naval Undersea Warfare Center Division
Newport, Rhode Island

DISCLAIMER NOTICE

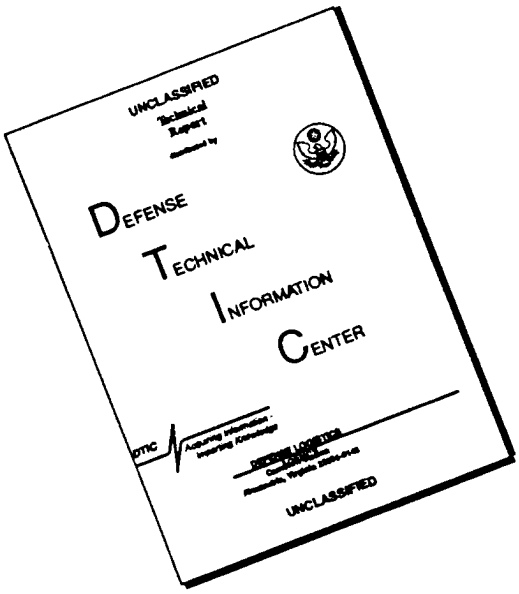

THIS DOCUMENT IS BEST QUALITY AVAILABLE. THE COPY FURNISHED TO DTIC CONTAINED A SIGNIFICANT NUMBER OF PAGES WHICH DO NOT REPRODUCE LEGIBLY.

PREFACE

This report was prepared under NUWC Project Nos. D34714 and D38714, "Heavyweight and Lightweight Torpedo Programs"; the principal investigators are H. Weinberg (Code 31) and R. E. Keenan, Scientific Applications International Corporation. The sponsoring activity is the Naval Sea Systems Command (PMS-402 and PMS-406). Additional funding was provided by the Office of Naval Research (J. Simmen, ONR0321)

The technical reviewer for this report was R. L. Deavenport (Code 3114).

Reviewed and Approved: 15 April 1996

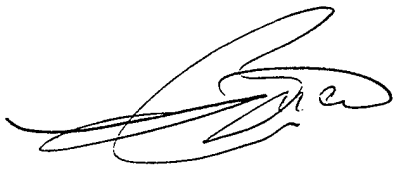

L. Bisci
Head, Weapons Systems Analysis Department

REPORT DOCUMENTATION PAGE

Form Approved
OMB No. 0704-0188

1. AGENCY USE ONLY *(Leave blank)*	2. REPORT DATE	3. REPORT TYPE AND DATES COVERED
	15 April 1996	

4. TITLE AND SUBTITLE

Gaussian Ray Bundles for Modeling High-Frequency Propogation Loss Under Shallow-Water Conditions

5. FUNDING NUMBERS

6. AUTHOR(S)

Henry Weinberg
Ruth E. Keenan

7. PERFORMING ORGANIZATION NAME(S) AND ADDRESS(ES)

Naval Undersea Warfare Center Division
1176 Howell Street
Newport, RI 02841-1708

8. PERFORMING ORGANIZATION REPORT NUMBER

TR 10,568

9. SPONSORING/MONITORING AGENCY NAME(S) AND ADDRESS(ES)

Naval Sea Systems Command (PMO-402, PMO-406)
2531 Jefferson Davis Highway
Arlington, VA 22242-5160

10. SPONSORING/MONITORING AGENCY REPORT NUMBER

11. SUPPLEMENTARY NOTES

12a. DISTRIBUTION/AVAILABILITY STATEMENT

Approved for public release; distribution is unlimited.

12b. DISTRIBUTION CODE

13. ABSTRACT *(Maximum 200 words)*

An acoustic propagation model was developed to analyze high-frequency propagation loss under shallow-water conditions. The model is based on Gaussian ray bundles, which are similar in form but somewhat simpler than Gaussian beams. After describing the approach, propagation loss predictions are compared with those of various "standard models" at lower frequencies, where the latter models are accurate and efficient. If Gaussian ray bundles compare well at the lower frequencies, they should perform well at the higher frequencies as ray approximations improve.

14. SUBJECT TERMS

Underwater Sound
Acoustic Propagation Models
Propagation Loss
Shallow-water Acoustics
Ray Theory

15. NUMBER OF PAGES
50

16. PRICE CODE

17. SECURITY CLASSIFICATION OF REPORT	18. SECURITY CLASSIFICATION OF THIS PAGE	19. SECURITY CLASSIFICATION OF ABSTRACT	20. LIMITATION OF ABSTRACT
Unclassified	Unclassified	Unclassified	SAR

TABLE OF CONTENTS

LIST OF ILLUSTRATIONS

GAUSSIAN RAY BUNDLES FOR MODELING HIGH-FREQUENCY PROPAGATION LOSS UNDER SHALLOW-WATER CONDITIONS

1. INTRODUCTION

This report introduces a range-dependent propagation loss model designed to support the simulation of high-frequency reverberation in shallow oceans. For simplicity, this discussion is confined to $N \times 2D$ environments. That is, environmental quantities such as the sound speed and bottom depth vary along vertical (r, z) planes through the source and field points, and out-of-plane scattering is neglected. The model is based on Gaussian ray bundles of the form

$$\Psi = \frac{\beta_0 \Gamma^2}{\sqrt{2\pi}\sigma p_r r} \exp\left\{-0.5\left[(z - z_v)/\sigma^2\right]\right\}, \tag{1}$$

where β_0 depends only on the source, Γ includes losses due to volume attenuation and boundary reflections, z_v is the depth along a central ray, p_r is the horizontal slowness, and σ, an effective standard deviation or half-beamwidth, is given by

$$\sigma = \frac{1}{2}\max(\Delta z, 8\lambda). \tag{2}$$

Here, Δz is the change in ray depth at constant range due to a change in source angle $\Delta\theta_0$, and λ is the wavelength at the field point.

If $\Delta z > 8\lambda$, σ confines most of the energy to the region between adjacent rays, while the 8λ minimum aperture prevents the acoustic pressure from growing too large near caustics, where

$$\lim_{\Delta\theta_0 \to 0} \frac{\Delta z}{\Delta\theta_0} = 0. \tag{3}$$

More sophisticated caustic corrections are often difficult to apply to realistic ocean conditions due to the numerical instability of various parameters or the violation of basic assumptions. For example, Ludwig's (reference 1) uniform asymptotic expansion involving the Airy function Ai and its derivative Ai′ applies to smooth caustics. There is a smooth transition between the oscillatory and damped behavior with large but finite values on the caustic itself. The expansion requires equation (3) to have a well-behaved first-order zero. This assumption is violated along rays that graze an ocean boundary because the limit in equation (3) fails to exist.

Equation (1) is based on conservation laws and appears to be consistent with Fresnel volume ray tracing (reference 2). Equation (2), on the other hand, was discovered by accident during the development of a Gaussian beam model.

A Gaussian beam (reference 3) is defined along a central ray by

$$P(s,\eta) = A\sqrt{c(s)/[rq(s)]} \times \exp\left(-i\omega\left\{\tau(s) + 0.5[p(s)/q(s)]\eta^2\right\}\right). \quad (4)$$

Again, r is the horizontal range, s is the arc length along the ray, η is the normal distance from the central ray, A is an arbitrary constant, ω is the radian frequency, $c(s)$ is the sound speed, and $p(s)$ and $q(s)$ are the beam curvature and beamwidth, respectively. The curvature and beamwidth satisfy a pair of ordinary differential equations that are integrated with the standard ray-tracing equations.

Gaussian ray bundles are somewhat easier to determine than Gaussian beams since σ is determined from adjacent rays at the field point, not by integrating differential equations. It is not known why the 8λ in equation (2) performs as well as it does. Hence, the bundles should be used with caution until σ can be placed on a firmer foundation, or until another model can be shown to provide a practical solution at the high frequencies of interest.

Several aspects of Gaussian ray bundles resemble the numerical integration of the one-way wide-angle Maslov-Chapman wavefield representation (reference 4). For example, transforming the Helmholtz equation from depth dependence to vertical slowness leads to a modified eikonal equation. The solution, a Legendre transform from depth to vertical slowness, serves as an algorithm, equation (31), to extrapolate ray bundle travel time to a field point. An important difference is that the present numerical integration of the pressure amplitude is based on power addition, not on coherent transforms.

Hardy (reference 5) suggested that a Gaussian form involving an experimentally determined standard deviation could be used to treat caustics. Although critics argued that one would have to conduct a separate experiment for every case of interest, it now appears that the single expression, equation (2), is sufficient. This will be demonstrated by several heuristic arguments in section 2.

Section 3 contains two propagation loss test cases. The first compares results with those of the Navy standards PE version 3.4 (reference 6) and ASTRAL version 4.2 (reference 7) at 25 and 10 kHz for a classic convergence zone. Then, the more academic models EFEPE (reference 8) and OASES (reference 9) are used to provide propagation loss at 1000 Hz for a shallow-water environment. If Gaussian ray bundles compare well with these "standards" at the lower frequencies, they should perform well at the higher frequencies, since the increase in frequency only improves the high-frequency approximation invoked by ray theory.

The ray segments used by the classical ray-tracing section are based on triangular sectors in which the inverse sound speed squared is a linear function of range and depth. The specific implementation, being somewhat different than previous implementations, is described in the appendix.

2. GAUSSIAN RAY BUNDLES

The original intent of this work was to evolve an $N \times 2D$ ray-tracing program into a Gaussian beam model. Development by evolution often gives additional insight. In this instance, it led to Gaussian ray bundles. Since rigorous proofs are not currently available, the justification relies on heuristic arguments. This section begins with a brief discussion of classical ray theory as a vehicle to introduce the notation. Gaussian ray bundles are constructed from classical rays in a number of ways, four of which are described below. The basic technique applies to a benign environment in which there are sufficient classical rays of a desired ray type to form well-behaved differences. The second technique is a *fallback* procedure in case there is only one classical ray of a particular type in the region of interest. Virtual rays are defined by unfolding classical rays to model propagation in the vicinity of the ocean boundaries. The last technique modifies the basic formula to model propagation at short ranges.

First consider the fan of n rays in figure 1. Parameters that describe the ν-th ray are subscripted by $(\,)_\nu$, while $(\,)_0$ refers to a point source with radian frequency ω at $(0, z_0)$. Accordingly, P_0 denotes the acoustic pressure at a reference distance r_0 from the source. The ν-th ray is launched with source angle $\theta_{\nu,0}$ and crosses the field-point range r at depth z_ν and travel time T_ν.

The horizontal slowness and vertical slowness,

$$p_{r,\nu} = \cos \theta_\nu / c_\nu$$

and (5)

$$p_{z,\nu} = \sin \theta_\nu / c_\nu,$$

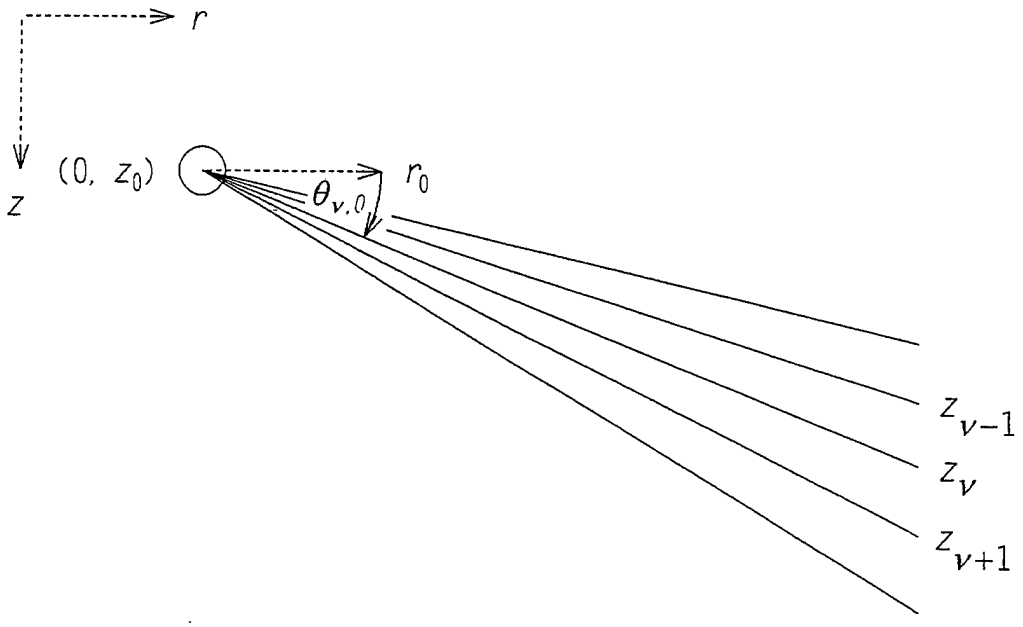

Figure 1. Fan of Acoustic Rays Launched from a Point Source

are defined in terms of the horizontal inclination angle θ_ν and the sound speed c_ν. Losses due to volume attenuation and boundary reflections are simulated by the pressure ratio Γ_ν and phase shift Φ_ν. Recall that the vertex velocity $p_{r,\nu}^{-1}$ is a ray invariant in range-independent environments.

Typical $N \times 2D$ ray-tracing programs require two types of spatial interpolations to model realistic ocean conditions. The first provides environmental data at discrete ranges along a vertical plane. The second interpolation provides environmental data at arbitrary points in the vertical plane so that ray trajectories can be evaluated analytically. In particular, if the inverse sound speed squared is found by linear interpolation within triangular sectors, the ray trajectories become parabolas. The implementation used here, being somewhat different than others, is described in the appendix.

The numerical implementation of geometrical spreading uses finite differences to estimate Δz_ν, the increment in ray depth at constant range due to an increment in source angle $\Delta\theta_{\nu,0}$. For this discussion, it is sufficient to use the central differences

$$\Delta z_\nu = (z_{\nu+1} - z_{\nu-1})/2, \tag{6}$$

$$\Delta\theta_{\nu,0} = (\theta_{\nu+1,0} - \theta_{\nu-1,0})/2 \tag{7}$$

for $\nu = 2, 3, \ldots, n-1$, and

$$\Delta z_1 = z_2 - z_1, \tag{8}$$

$$\Delta\theta_{1,0} = \theta_{2,0} - \theta_{1,0}, \tag{9}$$

$$\Delta z_n = z_n - z_{n-1}, \tag{10}$$

$$\Delta\theta_{n,0} = \theta_{n,0} - \theta_{n-1,0} \tag{11}$$

at the endpoints.

Later examples will demonstrate that the ocean boundaries will make the above definitions inappropriate for some Δz_ν. In anticipation of these boundary-induced complications, two depths $z_\nu^{(1)}$ and $z_\nu^{(2)}$ that bound z_ν are now introduced. Also, set

$$\Delta z_\nu = z_\nu^{(2)} - z_\nu^{(1)}. \tag{12}$$

Equation (12) will be equivalent to equations (6), (8), and (10) if the $z_\nu^{(1)}$ and $z_\nu^{(2)}$ are midpoints of the z_ν. That is,

$$z_\nu^{(1)} = (z_{\nu-1} + z_\nu)/2 \tag{13}$$

for $\nu = 2, 3, \ldots, n$, and

$$z_\nu^{(2)} = (z_\nu + z_{\nu+1}) / 2 \tag{14}$$

for $\nu = 1, 2, \ldots, n - 1$. The remaining depths,

$$z_1^{(1)} = (3z_1 - z_2) / 2 \tag{15}$$

and

$$z_n^{(2)} = (3z_n - z_{n-1}) / 2, \tag{16}$$

are obtained by reflecting $z_1^{(2)}$ about z_1 and $z_n^{(1)}$ about z_n.

Under the $N \times 2D$ and geometric-acoustic approximations, the contribution of the ν-th ray to the total field can be estimated from

$$P_\nu = r_0 P_0 \Gamma_\nu \left| \frac{p_{r,\nu} r \Delta z_\nu}{p_{r,\nu,0} \Delta \theta_{\nu,0}} \right|^{-1/2} \exp(i\omega T_\nu + i\Phi\nu), \tag{17}$$

if

$$z_\nu^{(1)} < z < z_\nu^{(2)}, \tag{18}$$

or if

$$z_\nu^{(2)} < z < z_\nu^{(1)} \tag{19}$$

and is zero otherwise. Each nontrivial P_ν corresponds to an eigenray, that is, a ray path that connects the source and field point. The underlying concept of classical ray theory is that the acoustic pressure P_c at any given field point is the coherent addition

$$P_c = \sum_\nu P_\nu \tag{20}$$

of eigenrays. The power addition

$$|P_c|^2 = \sum_\nu |P_\nu|^2 \tag{21}$$

is a smoother representation and better suited to many practical applications. Both summations include all nonzero values of P_ν.

Figure 1 is deceptively simple in that there is only one eigenray per field point. In other words, there is only one nonzero P_v. In general, the task of identifying all the eigenrays is difficult, especially in a range-dependent environment. To demonstrate this fact, it is convenient to define *ray type* as the number of surface and bottom reflections and upper and lower vertices. For example, the primary eigenrays for an isovelocity, flat-bottom environment consist of the direct path, the one surface bounce path, the one bottom bounce path, the one bottom then surface bounce path, and the one surface then bottom bounce path, illustrated in the upper portion of figure 2. The upper portion of figure 3 illustrates the continuous, predictable manner in which the angles of these ray paths vary with field-point depth at a 0.463-km (0.25-nmi) range.

The possible number of primary eigenrays in a range-dependent environment is unlimited, and the task of identifying all the eigenrays can be formidable. The lower portions of figures 2 and 3 show how quickly the number of eigenrays can multiply just from varying the bathymetry for this isovelocity environment. In this example, the direct and surface bounce paths are unaffected, but the number of bottom bounce paths has increased from three paths to nine paths for the 60.96-m (200-ft) field-point depth (figure 2). The arrival angle structure (figure 3) shows how the number of paths changes with field-point depth.

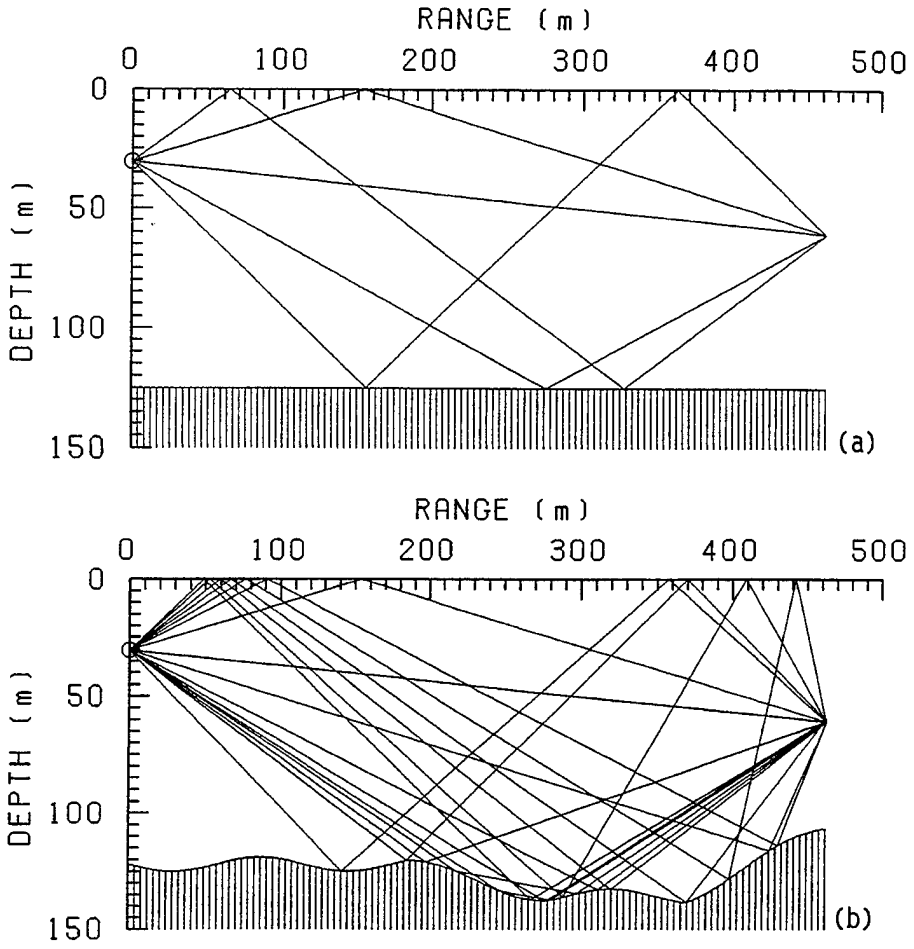

Figure 2. Primary Eigenrays to a 0.25-nmi, 100-ft Field Point in an Isovelocity Environment: (a) Flat and (b) Range-Dependent Bathymetry

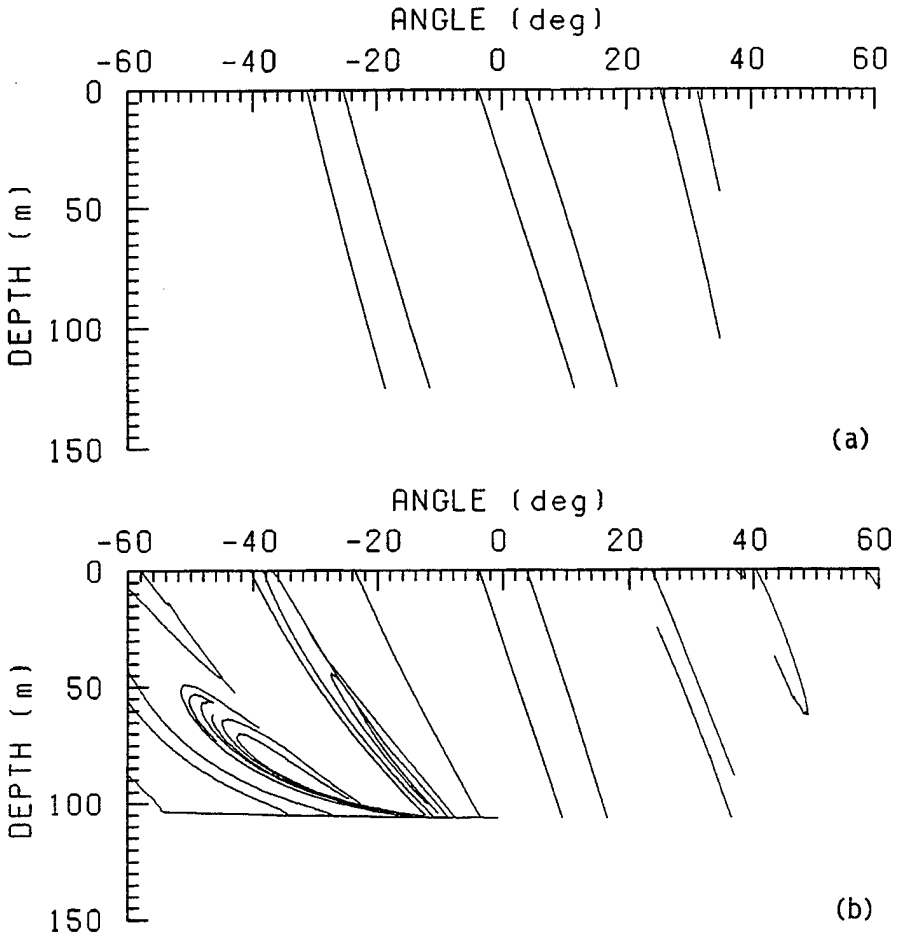

Figure 3. Arrival Angles vs Depth at 0.25 nmi in an Isovelocity Environment: : (a) Flat and (b) Range-Dependent Bathymetry

Using the same notation as before, the amplitude of the Gaussian ray bundle is now defined by

$$\Psi_\nu = \frac{\beta_{\nu,0}\Gamma_\nu^2}{\sqrt{2\pi}\sigma_\nu p_{r,\nu} r}\exp\left\{-0.5\left[\left(z-z_\nu\right)/\sigma_\nu\right]^2\right\}, \tag{22}$$

where

$$\beta_{\nu,0} = r_0^2 p_{r,\nu,0}\Delta\theta_{\nu,0}P_0^2 \tag{23}$$

depends only on the source, and where

$$\sigma_\nu = \frac{1}{2}\max\left(\Delta z_\nu, 8\lambda\right) \tag{24}$$

is an effective standard deviation or half beamwidth, and λ is the wavelength at the field point. The factor $\beta_{\nu,0}$ was chosen so that the energy within a geometric-acoustic ray tube equals the energy within a Gaussian ray bundle. Equation (24) was found by accident, as will be described shortly.

To find eigenrays, classical ray models typically perform an iterative search on test rays or interpolate in range or depth between test rays. The solution is local. If equation (17) is used, a classical eigenray is determined from a test ray that roughly falls within $\Delta z_\nu/2$ of the field-point depth at the field-point range. In contrast, ray bundles are global, affecting all depths to some degree. It is assumed that the Gaussian eigenray amplitude is formed by the power addition

$$\Psi_e = \sum_\nu \Psi_\nu \tag{25}$$

of bundles of the same type. The eigenray source angle $\theta_{e,0}$, horizontal slowness $p_{r,e}$, vertical slowness $p_{z,e}$, boundary phase shift Φ_e, and travel time T_e are obtained from the weighted averages:

$$\theta_{e,0} = \Psi_e^{-1} \sum_\nu \Psi_\nu \theta_{\nu,0}\,, \tag{26}$$

$$p_{r,e} = \Psi_e^{-1} \sum_\nu \Psi_\nu p_{r,\nu}\,, \tag{27}$$

$$p_{z,e} = \Psi_e^{-1} \sum_\nu \Psi_\nu p_{z,\nu}\,, \tag{28}$$

$$\Phi_e = \Psi_e^{-1} \sum_\nu \Psi_\nu \Phi_\nu\,, \tag{29}$$

$$T_e = \Psi_e^{-1} \sum_\nu \Psi_\nu T_{z,\nu}\,. \tag{30}$$

To obtain a more accurate expression for travel time, the ray bundle travel time T_ν is extrapolated to the field-point depth z by

$$T_{z,\nu} = T_\nu + p_{z,\nu}(z - z_\nu) \tag{31}$$

in equation (30) before the Gaussian weighting function is applied. Justification for the extrapolation in equation (31) is based on the relationship

$$\frac{\Delta T_\nu}{\Delta z_\nu} \approx p_{z,\nu} \tag{32}$$

and figure 4. The Gaussian eigenray amplitude

$$A_e = \sqrt{\Psi_e} \tag{33}$$

and field-point angle

$$\theta_e = \tan^{-1}\left(\frac{p_{z,e}}{p_{r,e}}\right) \tag{34}$$

yield the complex valued eigenray pressure

$$P_e = A_e \exp\left(i\omega T_e + i\Phi_e\right). \tag{35}$$

An additional complication makes it necessary to compute two weighted averages for each ray type. The first is the contribution from ray bundles with $\Delta z_v > 0$, the second with $\Delta z_v \leq 0$. Ray bundles must be separated in order to simulate the reversals in test ray depth versus source angle. These reversals are caustics that may be formed by the environment or by numerical approximations. In the isovelocity, flat-bathymetry case shown in figure 3, the arrival angle versus depth curve is monotonic for each ray type. (It was convenient to display arrival angle versus depth instead of test ray depth versus source angle. The two are equivalent in the isovelocity, flat-bathymetry case.). In contrast, the range-dependent bathymetry produces many reversals.

For simplicity, the current model assumes that caustics occur at turning points. Hence, the ray-tracing algorithm adds $-\pi/2$ to the phase shift Φ_v at each upper and lower vertex. Asymptotic theory dictates that the eigenray phase shifts Φ_e corresponding to the $\Delta z_v > 0$ and $\Delta z_v \leq 0$ weighted averages be separated by an additional $\pi/2$. These assumptions are not valid in many environments, and the coherent predictions are subject to errors. However, since the primary purpose of the model is to simulate high-frequency reverberation by power addition, phase errors are a secondary concern.

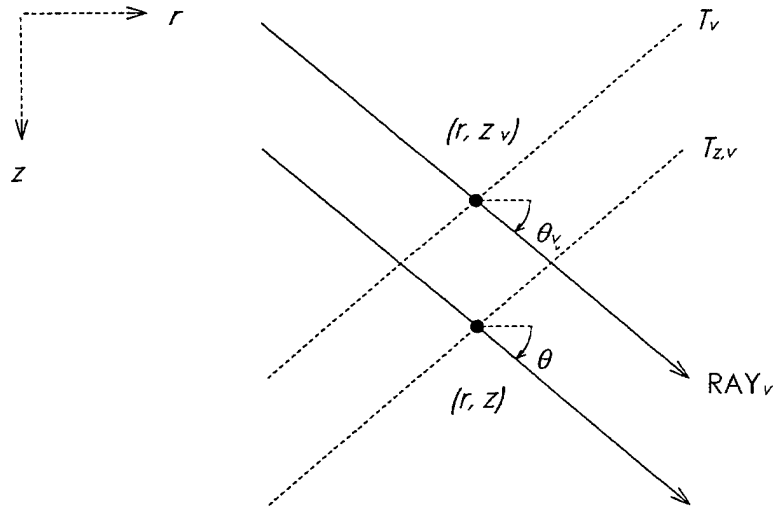

Figure 4. CASS Travel Time Interpolation

If $\Delta z_\nu/\Delta\theta_{\nu,0}$ is slowly varying, and equation (24) is simplified to

$$\sigma_\nu = \Delta z_\nu/2 \tag{36}$$

then classical eigenrays can be approximated by Gaussian eigenrays with a high degree of accuracy. In other words, Gaussian eigenrays can be made as accurate as classical eigenrays. This claim is suggested by figure 5, which shows $|P_e/P_c|^2$ for various values of n.

When $n = 1$, the ratio reduces to

$$\frac{\Psi_1}{|P_1|^2} = \sqrt{\frac{2}{\pi}}\exp\left\{-0.5\left[\left(z-z_1\right)/\sigma_1\right]^2\right\}. \tag{37}$$

The rectangular curve in figure 5a,

$$\begin{cases} 1 \text{ if } z_1 - \Delta z_1/2 < z < z_1 + \Delta z_1/2 \\ \\ 0 \text{ otherwise} \end{cases}, \tag{38}$$

provides a useful comparison. Equation (23) for $\beta_{\nu,o}$ sets the area under the Gaussian curve to the area under the rectangular curve.

According to equation (37), the Gaussian and rectangular curves differ by a factor of $\sqrt{2/\pi} \approx 0.80$ or -1 dB at $z = z_1$. The factor improves to 1.01 or 0.06 dB at the midpoint depth z_2 in figure 5b. Here, the contributions from three adjacent bundles are added, assuming that the increments in $\theta_{\nu,0}$ and z_ν are constant. Figure 5c shows the effects of doubling the number of bundles from three to six by cutting the increment in $\theta_{\nu,0}$ in half. Although the overall fit is significantly better, fluctuations in the vicinity of the midpoint depth remain at 0.06 dB. Figure 5c suggests that the Gaussian-induced fluctuations could be reduced by an averaging algorithm. This is borne out by figure 6, which averages two results. The source angles of the second are midpoints of the first. In short, energy is conserved in a single ray bundle, but an adequate description of the acoustic pressure requires the superposition of several.

The standard deviations σ_ν must be bounded from below to prevent the amplitudes Ψ_ν from growing too large in the vicinity of caustics. This bound will now be estimated for a well-known test case developed by Pederson and Gordon (reference 10) to investigate extreme downward refraction. Figure 7 contains their sound speed profile and ray diagram for a 0.9144-km (1000-yd) source depth. The inverse sound speed squared is linear in depth, so one can express ray trajectories in closed form. However, the results below do not use this feature and may be contaminated to a small degree by numerical artifacts. It should also be noted that the example does not represent realistic ocean conditions in that the sound speed is too small throughout most of the water column.

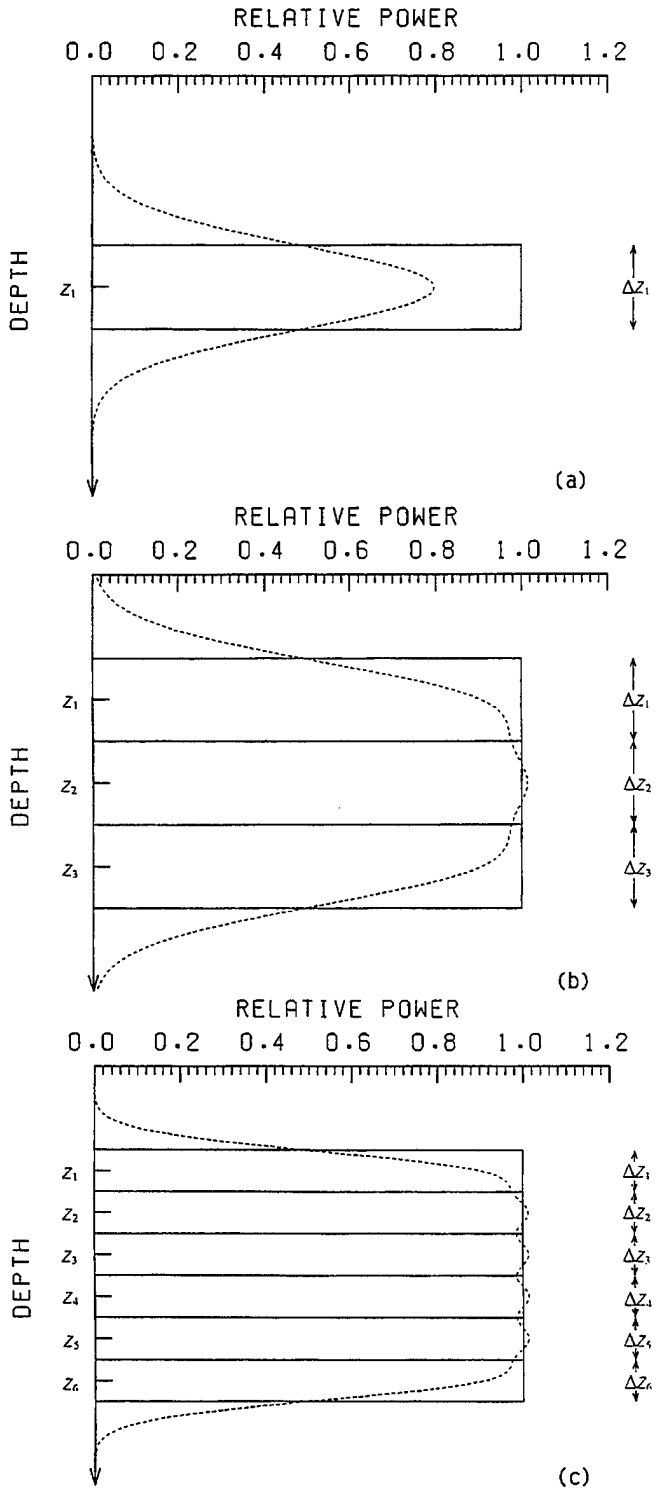

Figure 5. Power Addition of Gaussian Ray Bundles Normalized by the Geometric-Acoustic Pressure Squared

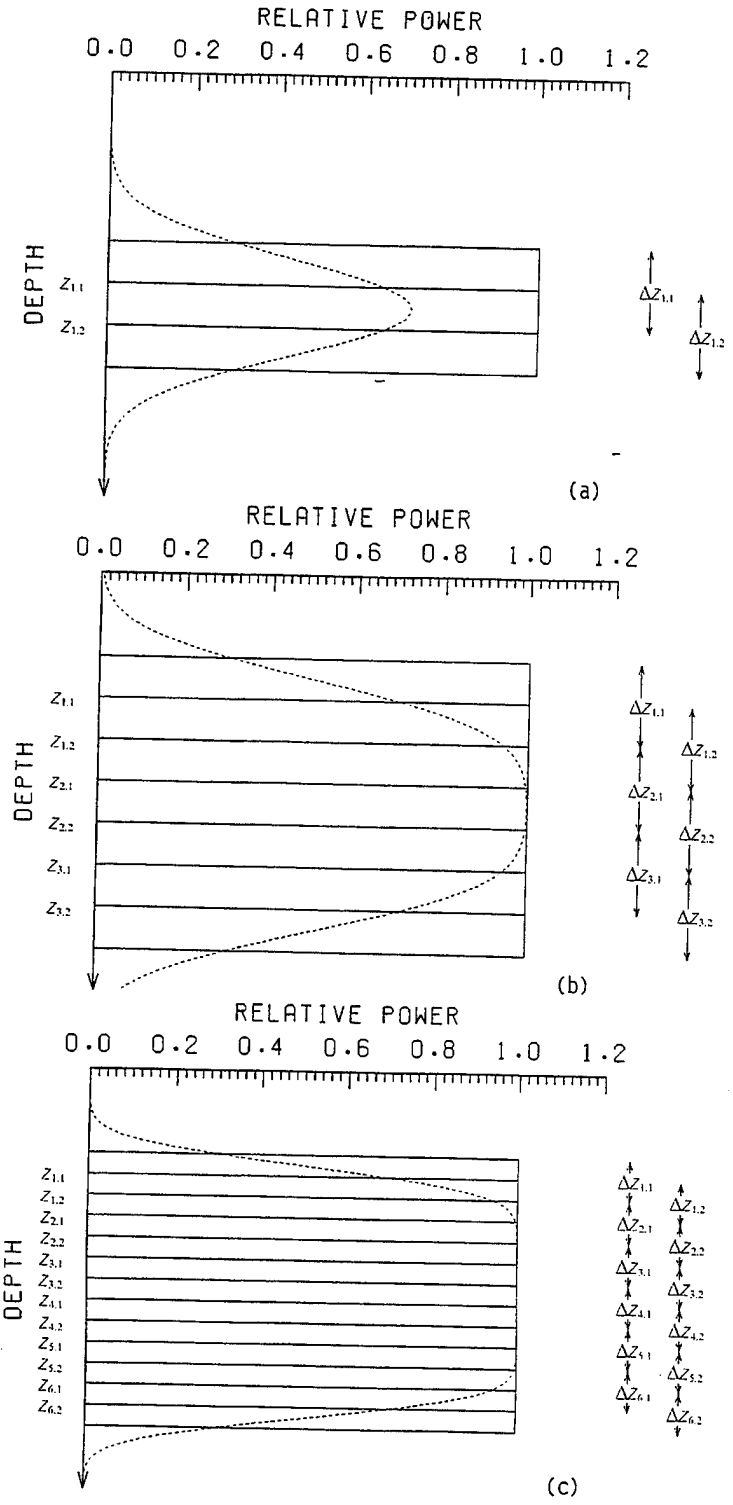

Figure 6. Averaged Value of Gaussian Bundle and Gaussian Bundle Offset by One Standard Deviation

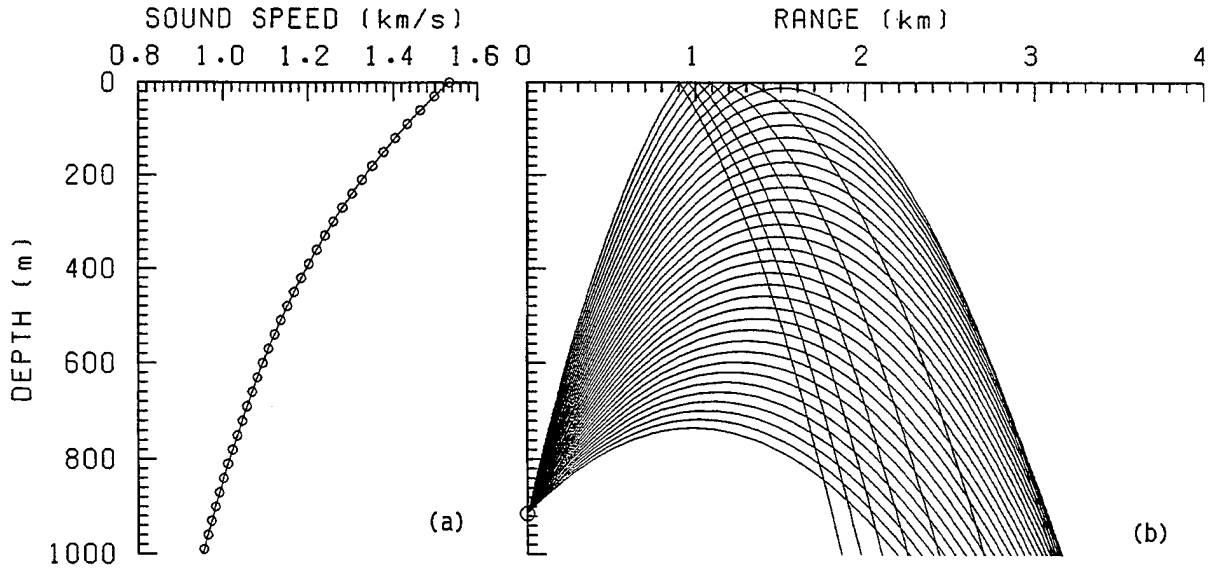

Figure 7. Formation of a Caustic Under Extreme Downward Refracting Conditions: (a) Sound Speed Profile and (b) Ray Diagram for a 0.9144-km (1000-yd) Source Depth

Figure 8 illustrates the effect of changing the lower bound of σ on propagation loss for a 0.7315-km (800-yd) field-point depth in the vicinity of the caustic at 2.89 km. Decibel levels were computed by coherent eigenray addition for

$$\sigma_\nu = \begin{cases} \frac{1}{2}\max(\Delta z_\nu, \lambda) & \text{(a)} \\ \frac{1}{2}\max(\Delta z_\nu, 8\lambda) & \text{(b)} \\ \frac{1}{2}\max(\Delta z_\nu, 4\pi\lambda) & \text{(c)} \\ \frac{1}{2}\max(\Delta z_\nu, 16\lambda) & \text{(d)} \\ \frac{1}{2}\max(\Delta z_\nu, 32\lambda) & \text{(e)} \end{cases}. \tag{39}$$

In figure 8a, σ_ν is too small. Although bounded, the level is too high in the illuminated region to the left of the caustic and falls off too rapidly in the shadow zone to the right of the caustic. The opposite occurs in figure 8e, where σ_ν is too large; now the decibel level is too small at the caustic and falls off too slowly in the shadow zone. Equation (24) is currently based on figure 8b because it currently gives the best overall performance near the caustic for both coherent and power additions. Evidence to be provided later will indicate that this remarkably simple formula is far

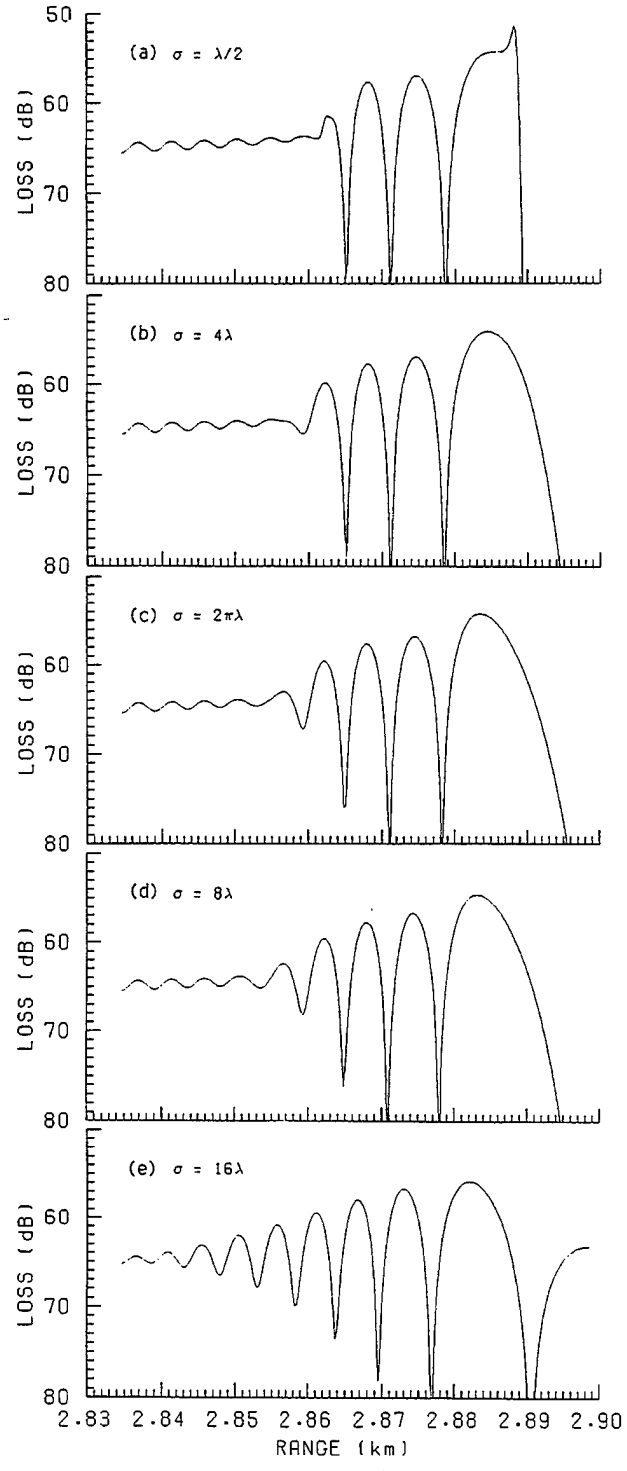

Figure 8. Propagation Loss vs Range in the Vicinity of a Caustic for a 0.9144-km (1000-yd) Source Depth, 0.7315-km (800-yd) Field-Point Depth, and Various Lower Bounds of σ: (a) λ/2, (b) 4λ, (c) 2πλ, (d) 8λ, (e) 16λ

more general than would be expected. Note that figures 8c and 8d are closer to the generally accepted answer in the vicinity of 2.86 km. Since this range is dominated by the ray that grazes the ocean surface, it is likely that a phase error was produced by the treatment of boundary reflections, which topic is treated next.

As is customary in typical ray-tracing models, rays are attenuated at the ocean boundaries by appropriate reflection coefficients. The cumulative effect is contained in the pressure ratio

$$\Gamma_\nu = \prod \gamma_{s,\nu} \times \prod \gamma_{b,\nu} \tag{40}$$

and phase shift

$$\Phi_\nu = \sum \phi_{s,\nu} + \sum \phi_{b,\nu} , \tag{41}$$

where $\gamma_{s,\nu}$ and $\gamma_{b,\nu}$ denote surface and bottom reflection coefficient amplitudes, respectively, and $\phi_{s,\nu}$ and $\phi_{b,\nu}$ are the corresponding phase shifts. Specific examples of reflection coefficients appear in later sections.

The ocean boundaries impose additional requirements on the numerical computation of both classical and Gaussian eigenrays. Although the difficulties discussed below stem from tracing rays to a constant range, it is felt that the benefits of *stepping* in range overshadow any disadvantages.

First consider a constant sound speed environment. The range r and field point to source depth z - z_0 for the direct path are related by

$$z - z_0 = r \tan \theta_0 . \tag{42}$$

Holding r constant, the differential

$$dz = r \sec^2 \theta_0 d\theta_0 \tag{43}$$

provides the lower bound

$$\Delta z_\nu \geq r \Delta \theta_{\nu,0} \tag{44}$$

for the change in ray depth with source angle. In other words, if the angular spacing between tests rays is too large, there will be only one direct path at the range of interest. It will not be possible to compute the required increments Δz_ν and $\Delta \theta_{\nu,0}$. Realistic ocean conditions create additional complications.

If computer run time is not a concern, and the sound speed and bottom are well behaved, one can make $\Delta \theta_{\nu,0}$ sufficiently small that several rays of the same type cross the range of interest. The practical approach taken here uses

$$z_\nu^{(1)} = z_\nu - \Delta z_\nu / 2,$$
$$z_\nu^{(2)} = z_\nu + \Delta z_\nu / 2 \tag{45}$$

instead of equations (13)-(16) to set the bounding depths $z_\nu^{(1)}$ and $z_\nu^{(2)}$, where

$$\Delta z_\nu = z_b - z_s \tag{46}$$

is the difference between the bottom and surface depths at range r. Since adjacent rays of the same type are unavailable, the Gaussian bundle distributes its energy normally about the central ray with a standard deviation of half the water column.

It is often possible to create adjacent rays of a desired type by unfolding rays of an adjacent type. To demonstrate the importance of these virtual rays, consider an eigenray that is incident to a field point slightly above the ocean bottom as shown in figure 9. Circles along the vertical dashed line represent the depths at which a fan of reflected test rays cross the field point range r, with ray ν being the closest to the bottom. Besides denoting range, the horizontal axis also serves to illustrate the relative amplitude of a Gaussian ray bundle that is centered at z_ν and has a standard deviation of $\sigma = |\Delta z_\nu|/2$. The unshaded portion represents reflected energy that does not contribute to the incident eigenray. Unless unfolded, power due to the shaded portion will be lost to the bottom, and the eigenray's amplitude will be too small. By projecting the bundle along incident rays, it becomes clear that the shaded portion corresponds to incident energy.

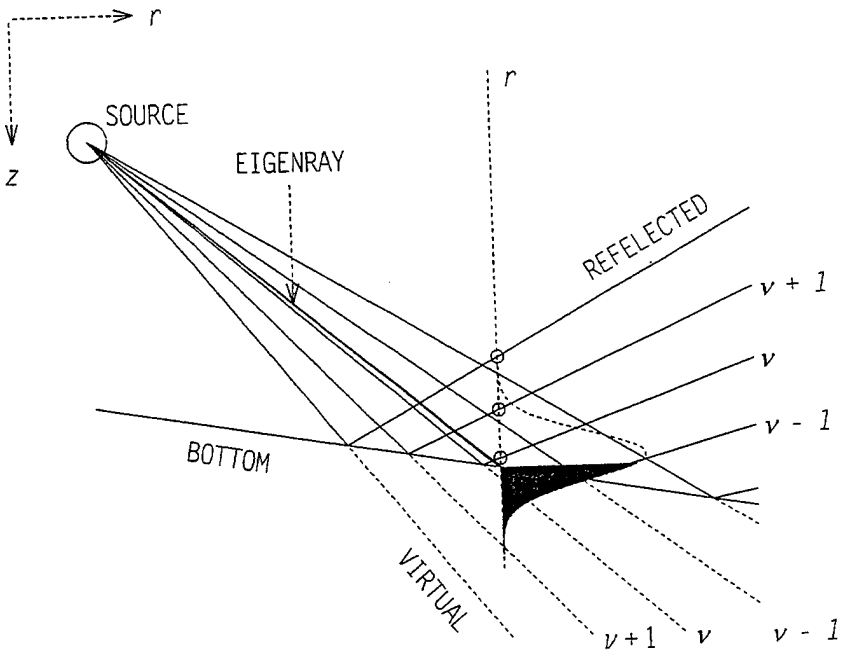

Figure 9. Creation of Virtual Rays by Unfolding Classical Rays at a Boundary

Except in the simplest cases, it is not clear how the virtual ray parameters $\theta'_{\nu,0}$, $p'_{r,\nu}$, $p'_{z,\nu}$, Φ'_ν, T'_ν, Ψ'_ν should be unfolded from their real counterparts. To avoid the cumbersome task of adding or removing the effects of boundary reflection coefficients during the unfolding process, the current procedure sets

$$\begin{aligned}
\theta'_{\nu,0} &= \theta_{\nu,0}, \\
p'_{r,\nu 0} &= p^*_{r,\nu}, \\
p'_{z,\nu 0} &= p^*_{z,\nu}, \\
\Psi'_\nu &= \Psi_\mu, \\
T'_\nu &= T_\nu, \\
\Phi'_\nu &= \Phi_\mu,
\end{aligned} \tag{47}$$

where the asterisk (*) indicates a reflection about the appropriate boundary and μ is the ray index nearest to ν such that ray μ and the eigenray are of the same type. Errors in virtual ray parameters increase with distance to the boundary. However, the distance from the virtual ray to the field point also increases, so that the effect on the eigenray decreases.

For example, referring once again to figure 9, one sees that $(p'_{r,\nu}, p'_{z,\nu})$ are the direction numbers of the dashed line for ray ν. The virtual ray amplitude and phase are obtained from ray ν - 1, the direct path ray nearest to ray ν.

A few other special cases require attention. For brevity, the discussion is limited to one such case—nearfield propagation. For the amplitude of the Gaussian ray bundle Ψ_ν to approach spherical spreading as the field point (r, z) approaches $(0, z_0)$, it is necessary that the standard deviation

$$\sigma_\nu \propto \Delta z_\nu \tag{48}$$

in the vicinity of the source. Unless equation (24) is adjusted, equation (44) indicates that the 8λ lower bound of σ_ν will be invoked for short ranges, such that

$$r \le \frac{\Delta z_\nu}{\Delta \theta_{\nu,0}} \le \frac{8\lambda}{\Delta \theta_{\nu,0}}. \tag{49}$$

The current adjustment replaces the 8λ in equation (24) with

$$\min\left(\frac{\pi r}{180}, 8\lambda\right). \tag{50}$$

One degree or $\pi/180$ radians was found to work better than $\Delta\theta_{\nu,0}$ in several test cases.

3. MODEL COMPARISONS

This section contains two sets of propagation loss test cases. For convenience, the Gaussian ray bundle based computer code has been given the acronym GRAB. The first test case compares GRAB results with those of the Navy standards PE V3.4 (reference 6) and ASTRAL V4.2 (reference 7) at 25 Hz and 10 kHz for a classic convergence zone. Then GRAB and the more academic models EFEPE (reference 8) and OASES (reference 9) are used to predict propagation loss at 1,000 Hz for a shallow-water environment. If GRAB compares well at these lower frequencies, it should also perform well above 20 kHz, the high frequencies of interest. We begin with a brief overview of the comparison models.

ASTRAL V4.2, a current Navy standard model for range-dependent environments, was designed for computational speed, frequencies less than 1 kHz and deep-water scenarios. ASTRAL bundles energy into 50-100 "shmodes" and provides a range- and depth-averaged intensity solution. (Shmodes are smooth mode-like functions that decay exponentially beneath their turning points.) The ASTRAL treatment of bottom interactions uses a weighted average of a reflected and a refracted path.

The parabolic equation (PE) was introduced into underwater acoustics in the early 1970s by Hardin and Tappert (reference 11). They devised an efficient numerical scheme based on Fourier transforms. PE techniques have grown and are now popular for solving range-dependent propagation problems. The Navy standard PE V3.4 model, a direct descendant of the original Hardin and Tappert work, uses split-step Fourier transforms in depth to compute the coherent pressure field. Numerical aliasing and phase errors limit the types of scenarios that can be modeled. In particular, shallow-water environments where the bottom properties represent an abrupt change from the water column should be avoided. As is typical of PE models, the computation time and storage requirements increase with frequency.

More robust PE solutions, such as Collins' finite element EFEPE model (reference 12) have been designed to bypass the split-step Fourier depth transform. This model is more accurate than the Navy standard PE V3.4 for bottom interacting scenarios and can treat higher angle energy. However, EFEPE does not incorporate volume attenuation into the water column, an important consideration at high frequencies. The stratified, geoacoustic bottom description must include a highly absorbing basement layer in order to simulate a radiation condition without introducing erroneous reflections.

OASES (Ocean Acoustic and Seismic Exploration Synthesis) models seismo-acoustic propagation in horizontally stratified waveguides using wave number integration in combination with direct global matrix techniques. The model is a more robust version of SAFARI (Seismo-Acoustic Fast field Algorithm for Range Independent environments) (reference 13). OASES includes shear properties in a layered, geoacoustic bottom and eliminates aliasing problems by moving the integration contour onto the complex plane, i.e., introducing artificial attenuation.

To avoid model/model comparison complications, the same submodels (surface loss, bottom loss, etc.) were used whenever possible. Since the bottom descriptions required by the GRAB,

EFEPE and the OASES model are sufficiently different, it was necessary to invoke an OASES option that generates a plane wave coefficient from bottom layers and implement these results into a GRAB bottom loss table. Range-dependent sound speed is not resolved so easily (reference 14). OASES, being range independent, is based on one sound speed profile. PE, ASTRAL, and EFEPE transition abruptly from one profile to another at user-provided ranges. Only GRAB models the sound speed continuously with range as described in section 2.

3.1 CLASSIC CONVERGENCE ZONE

GRAB predictions for a classic convergence zone were then compared with those of the Navy standard models ASTRAL V4.2 and PE V3.4. Both standard models should provide reasonable results, with PE being the more accurate of the two. The sound speed profile and ray trace for a 792.48-m (2600-ft) source depth and 13,716-m (15,000-ft) water depth appear in figure 10. GRAB, PE, and ASTRAL 25-Hz and 10-kHz propagation losses are contoured in figures 11, 12, and 13 respectively.

To highlight the formation of shadow zones and caustics, GRAB, PE, and ASTRAL were run without volume attenuation or bottom interacting energy. The GRAB prediction used random phase eigenray addition, sampled range in 1.852-km (1-nmi) increments, and employed a ±20° vertical aperture in 0.1° increments. ASTRAL also used a 1.852-km increment, while the full-field PE model automatically selected sampling parameters to avoid aliasing.

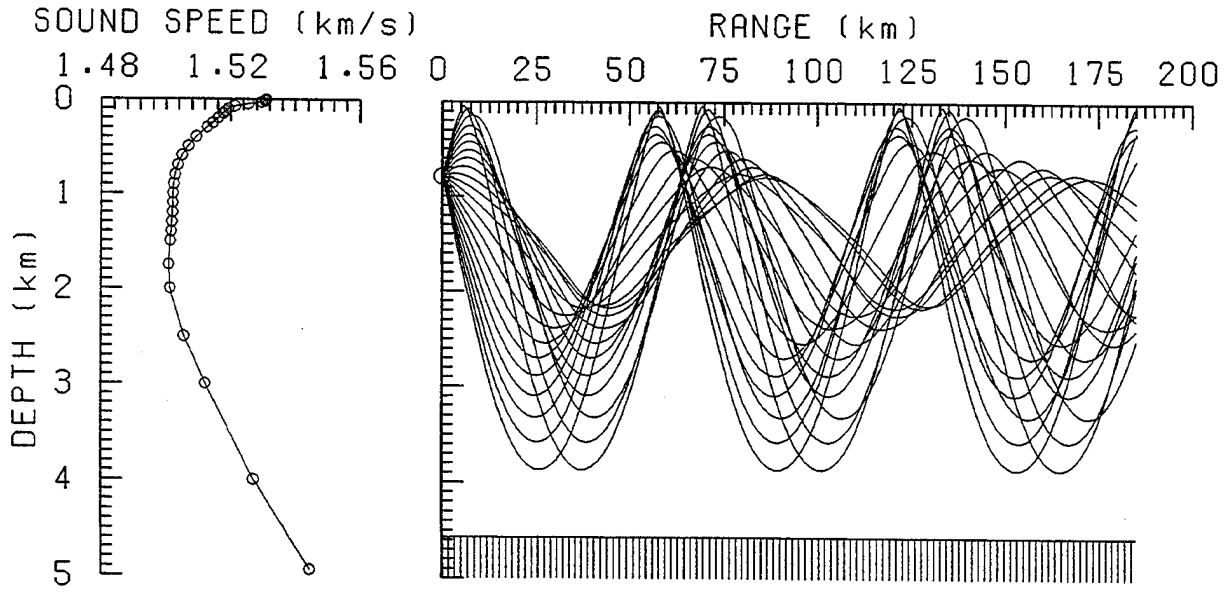

Figure 10. Classic CZ Environment: (a) Sound Speed Profile and (b) Ray Trace

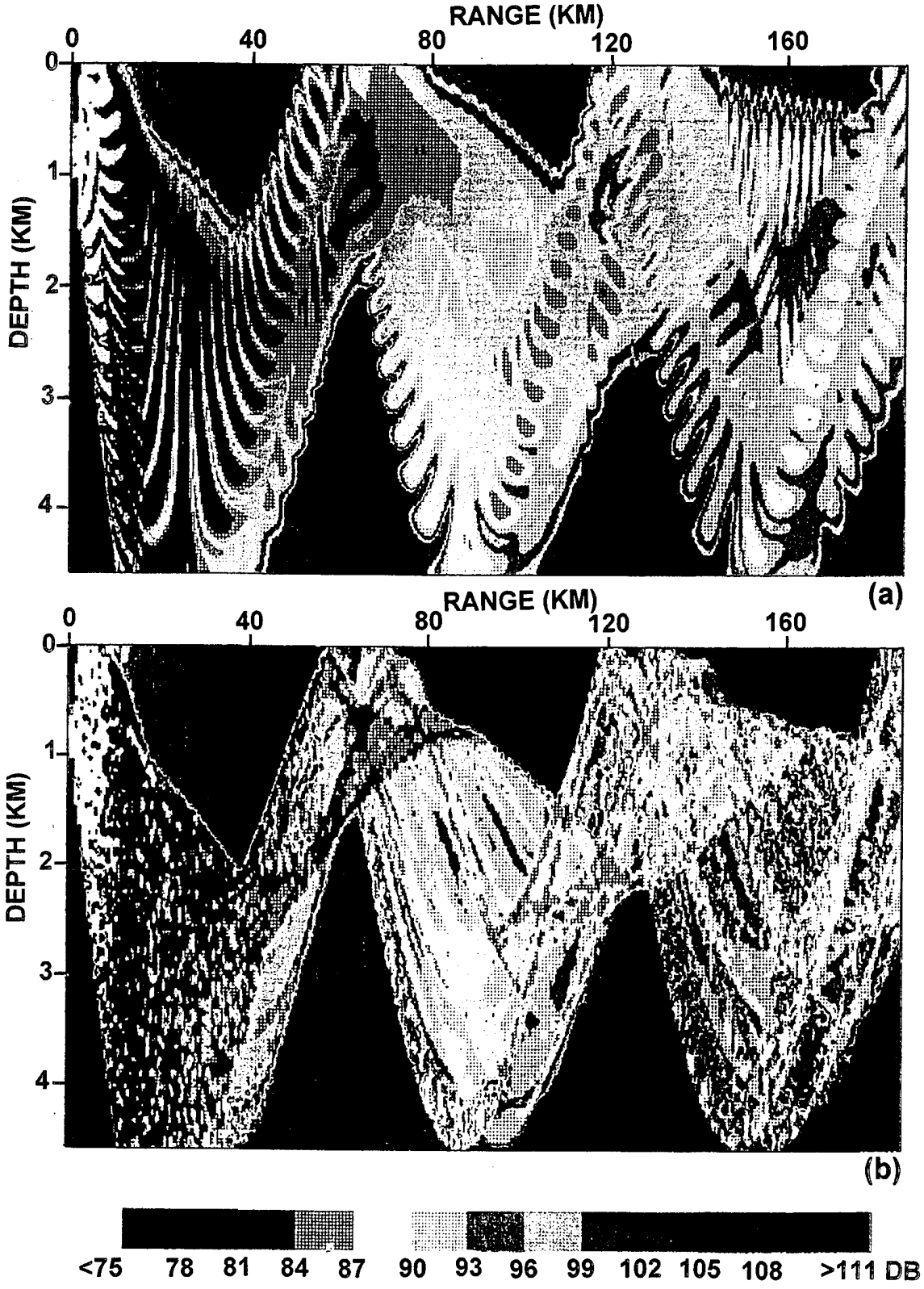

Figure 11. GRAB Propagation Loss Contours for Classic CZ Environment: (a) 25 Hz and (b) 10 Hz

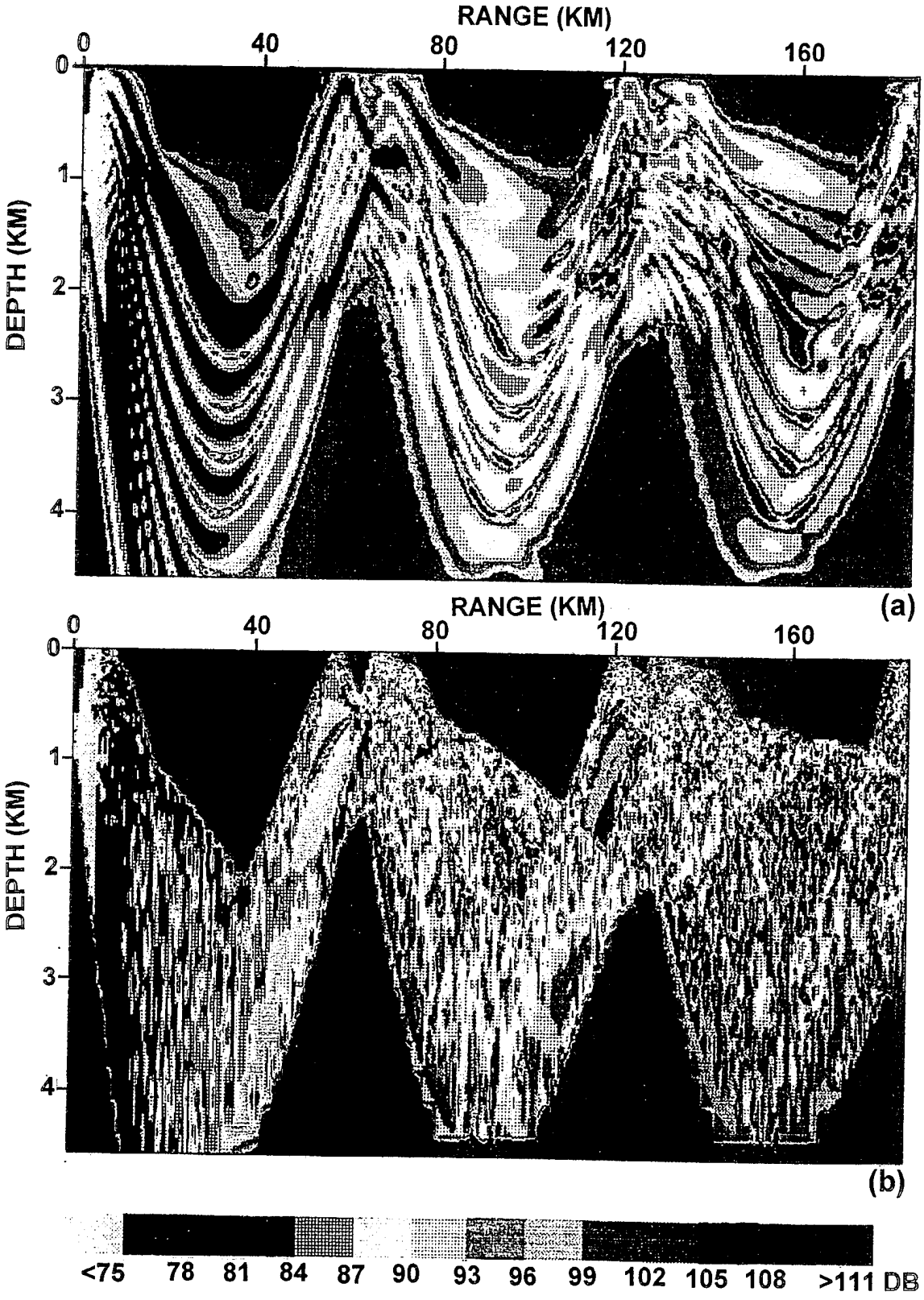

Figure 12. PE Propagation Loss Contours for Classic CZ Environment: (a) 25 Hz and (b) 10 kHz

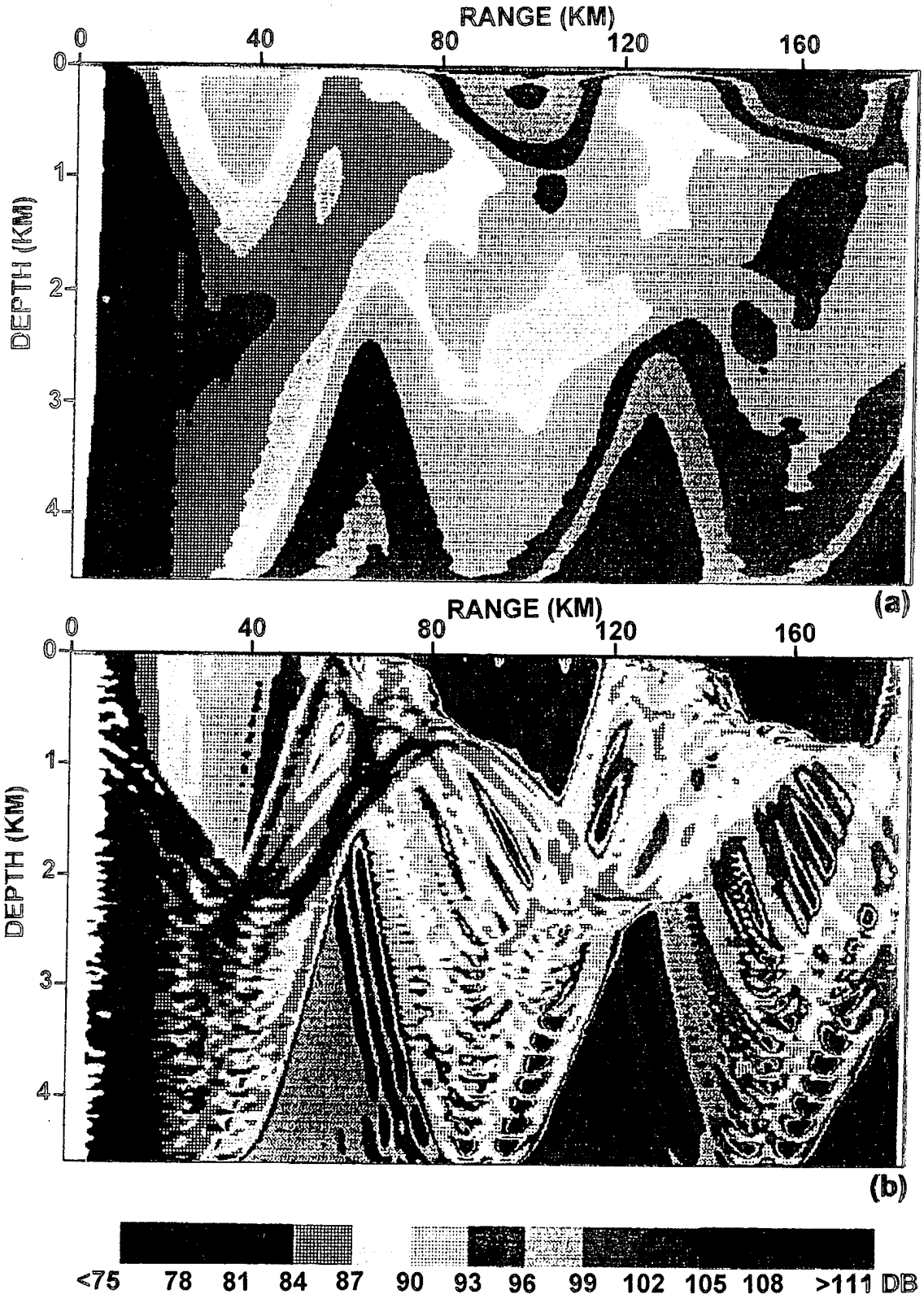

Figure 13. ASTRAL Propagation Loss Contours for Classic CZ Environment: (a) 25 Hz and (b) 10 kHz

Figure 14 displays GRAB, PE, and ASTRAL propagation loss versus range for a 792.48-m (2600-ft) receiver. Although GRAB was not designed for frequencies as low as 25 Hz, the model tracks the general trend very well and maintains the energy levels in the tails of the caustic. Table 1 compares the computation times of each model using a 50-MHz 386 IBM personal computer. A large percentage of the GRAB computation time is a result of input/output operations.

Table 1. Comparison of Computation Times

Model	Computation Time	
	25 Hz	10 kHz
GRAB	4.5 minutes	4.5 minutes
PE	6 seconds	26 hours
ASTRAL	5 seconds	5 seconds

3.2 SHALLOW-WATER ENVIRONMENT AT 1000 HZ

The next set of test cases compares GRAB, EFEPE, and OASES propagation-loss predictions for a shallow-water environment. Due to the high-frequency computation limitations of EFEPE and OASES, it was necessary to baseline GRAB at 1,000 Hz. It was assumed that the essential physics at 1000 Hz is the same as at 20 kHz, and that differences can be attributed to surface, volume, and boundary losses whose accuracy is independent of the propagation model.

For the model/model comparisons here, the environment consists of the sound speed profile in figure 15, a perfectly reflecting sea surface, and zero volume attenuation. The source and receiver depths are 30.48 m (100 ft). Since OASES is a range-independent model, predictions involving OASES assume a flat bottom at 152.4 m (500 ft) of all sand or all rock. After GRAB was baselined with OASES and EFEPE for this range-independent environment, GRAB and EFEPE predictions were compared for a downslope bathymetry. Ray diagrams for both cases are traced in figure 16.

3.2.1 Sand Bottom

The sand bottom parameters include a 1572-m/sec sediment sound speed, a 1.268-gm/cm^3 density, and an attenuation of 0.02 dB/λ or 0.03 dB at 1,000 Hz. These yield the bottom loss versus grazing angle curves in the upper portion of figure 17. GRAB exercised its Rayleigh reflection coefficient option, while EFEPE and OASES computed equivalent plane wave reflection coefficients for a finite and halfspace bottom, respectively.

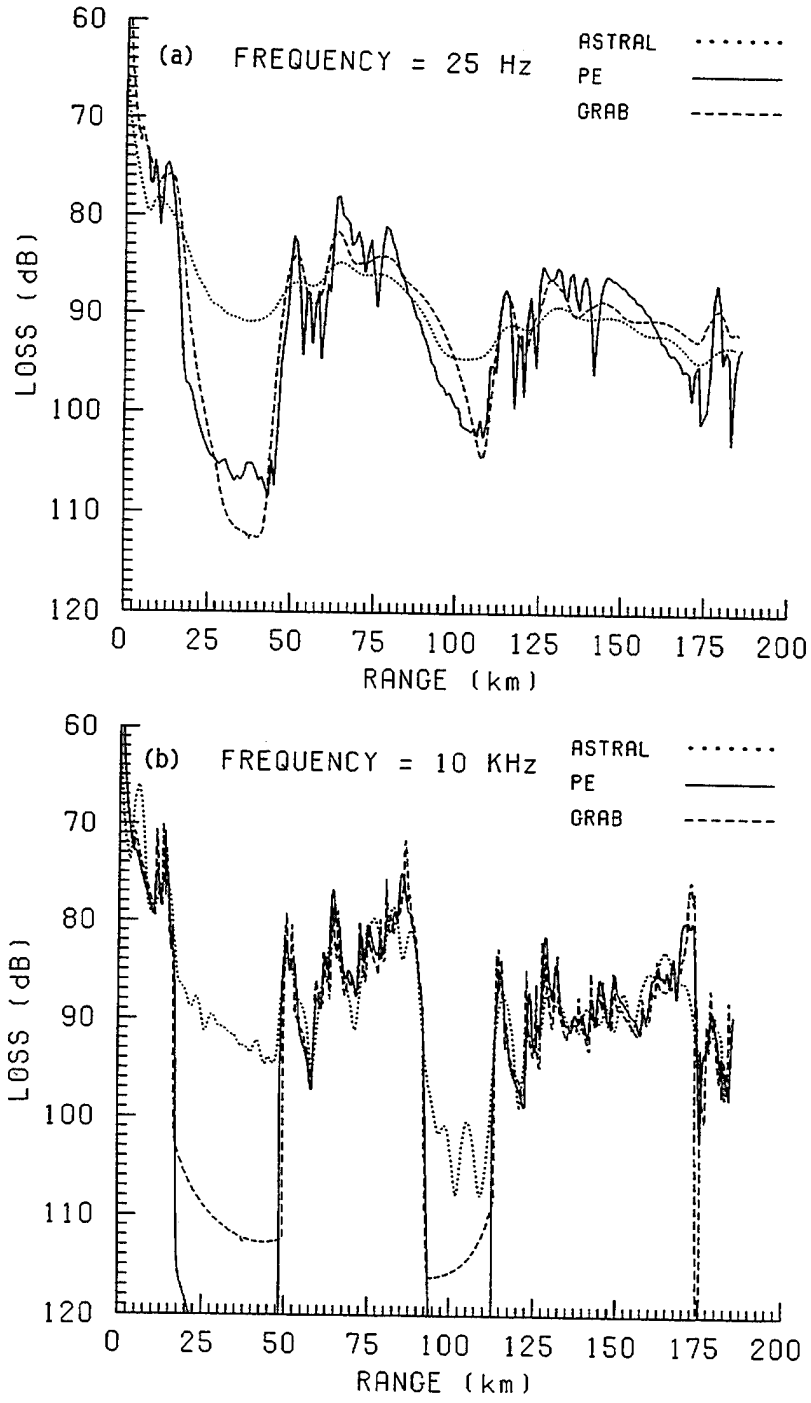

Figure 14. GRAB, PE, and ASTRAL Propagation Loss Predictions at a 2600-ft Receiver in a Classic CZ Environment: (a) 25 Hz and (b) 10 kHz

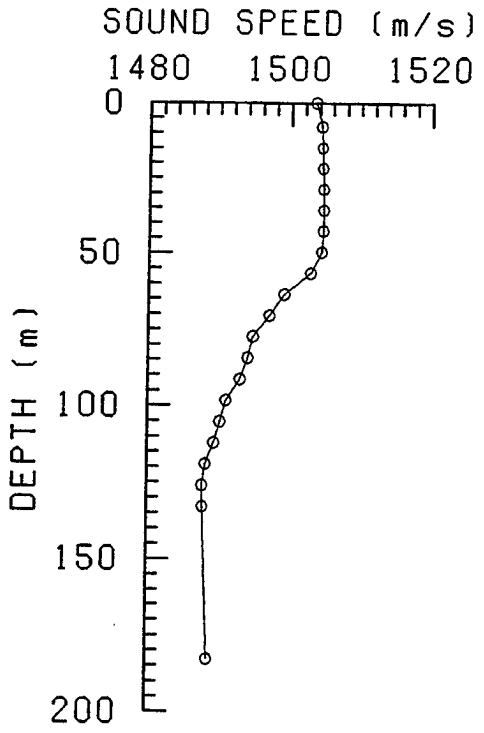

Figure 15. Shallow-Water Environment Sound Speed Profile

EFEPE and OASES propagation loss predictions are compared in figure 18. The EFEPE prediction used a 0.1-m depth mesh and a 1.5-m range step. Input phase velocities for the OASES wave number integrand spanned 1,000 to 8,000 m/sec, with the latter producing a 1.1-m range step. Although the EFEPE and OASES range steps are different, the two results are nearly identical.

Figure 19 compares the coherent GRAB prediction with the EFEPE prediction of figure 18. The GRAB range step is 10~m and its aperture is ±80° with test rays every 0.1°. The coherent GRAB levels differ from the EFEPE levels (and hence the OASES levels) by less than 1 dB at most ranges. Note the exceptional agreement between interference patterns.

3.2.2 Rock Bottom

The rock bottom is described by a 3750-m/sec sound speed, a 0.02-dB/λ attenuation, and 2.5-gm/cm^3 sediment density. GRAB, EFEPE, and OASES bottom loss functions for a rock bottom are shown in the lower portion of figure 17. Note that the sand bottom losses for grazing angles beyond 20° are highly attenuated, while propagation over rock is strong for grazing angles up to 80°. In this test case, an 80° source angle interacted with the bottom 50 times in 2.6 km. Thus, small differences in the bottom description become significant.

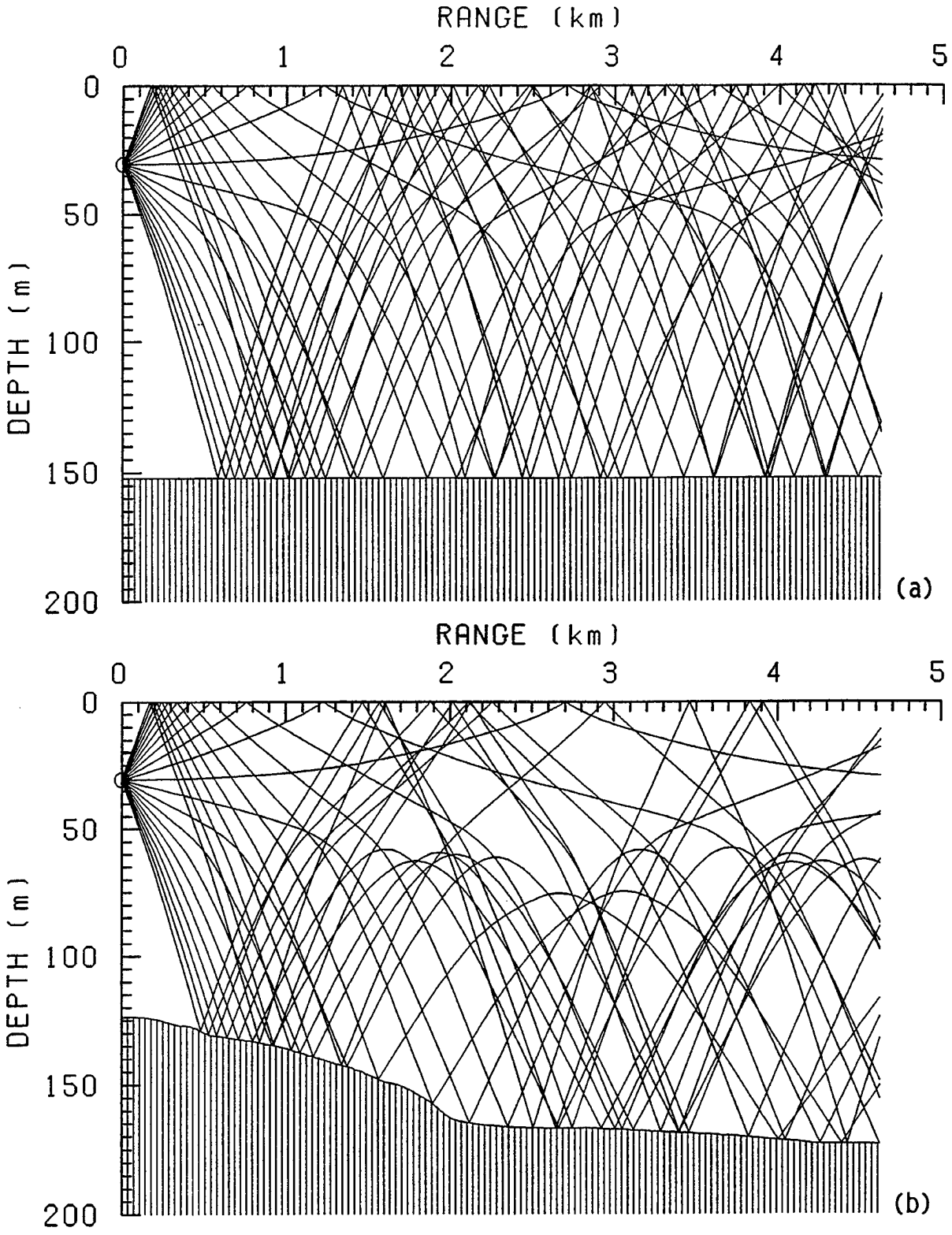

Figure 16. Shallow-Water Environment Ray Trace: (a) Flat 152.4-m (500 ft) and (b) Downslope Bathymetry

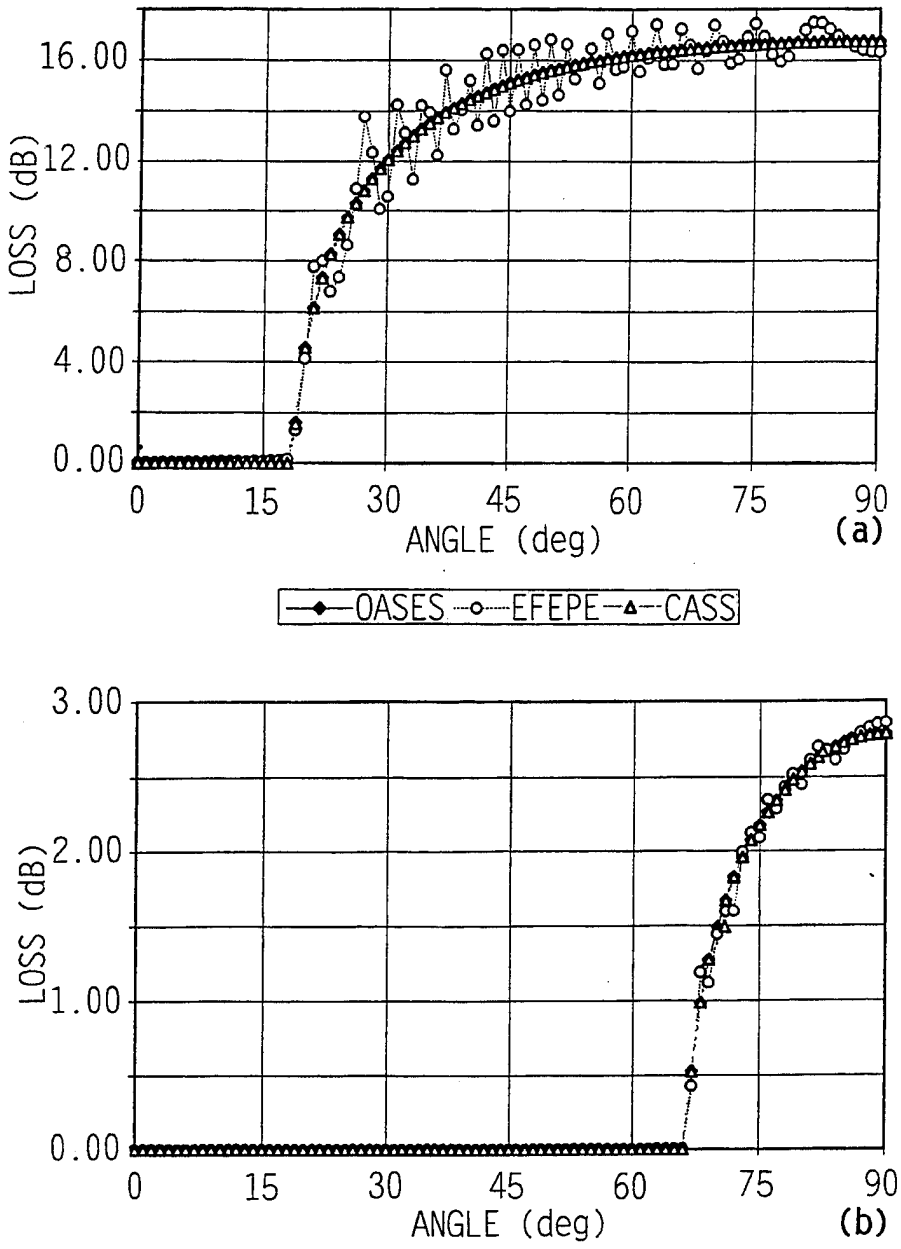

Figure 17. Bottom Forward Reflection Loss vs Angle at 1 kHz: (a) Sand and (b) Rock

Figure 20 illustrates the GRAB random and coherent propagation loss predictions with a 1.1-m range step and a ±80° aperture sampled every 0.1°. Because angles up to 80° are now important, the interference pattern is more complicated than it was for the sand bottom. To make meaningful comparisons, the intensity is averaged over a 0.1852-m (0.1-nmi) sliding range window. Figure 21 displays the results every 0.01852 m (0.01 nmi). As in the sand bottom case, EFEPE was run with a depth mesh of 0.1 m and a range step of 1.5 m, and the OASES range step for the phase velocity interval 1000 to 8000 m/sec is 1.1 m. Even with its better phase modeling, EFEPE results have phase errors due to high propagation angles. Nevertheless, the differences among the range-averaged GRAB, EFEPE, and OASES predictions are small.

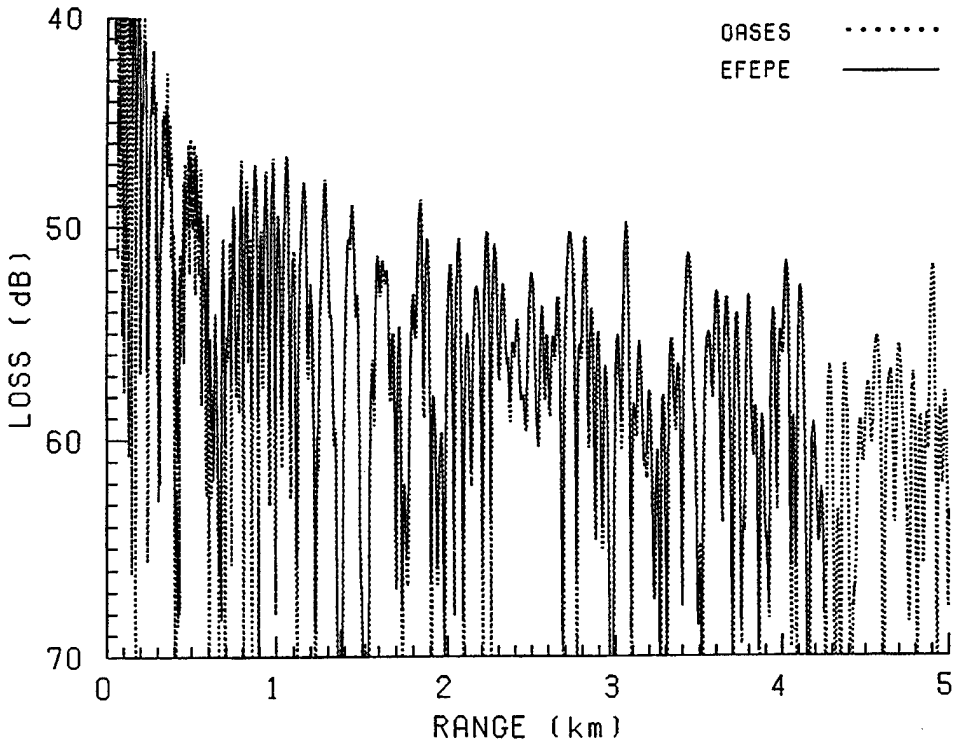

Figure 18. EFEPE and OASES Propagation Loss Predictions at 1 kHz for a Flat, Sandy Bottom

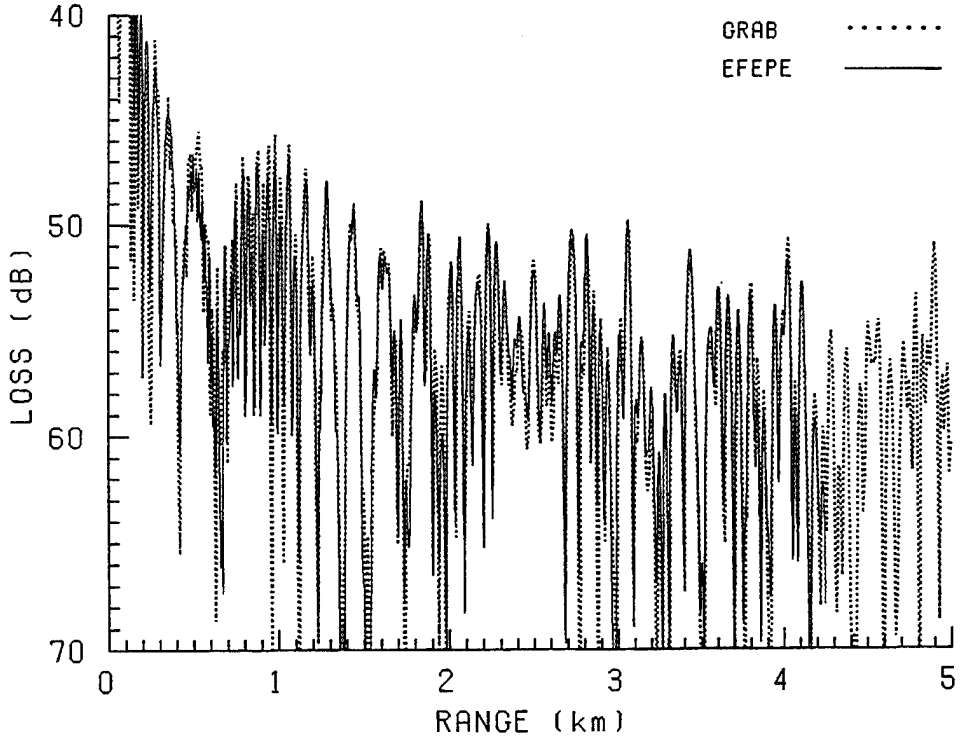

Figure 19. Coherent GRAB and EFEPE Propagation Loss Predictions at 1 kHz for a Flat, Sandy Bottom

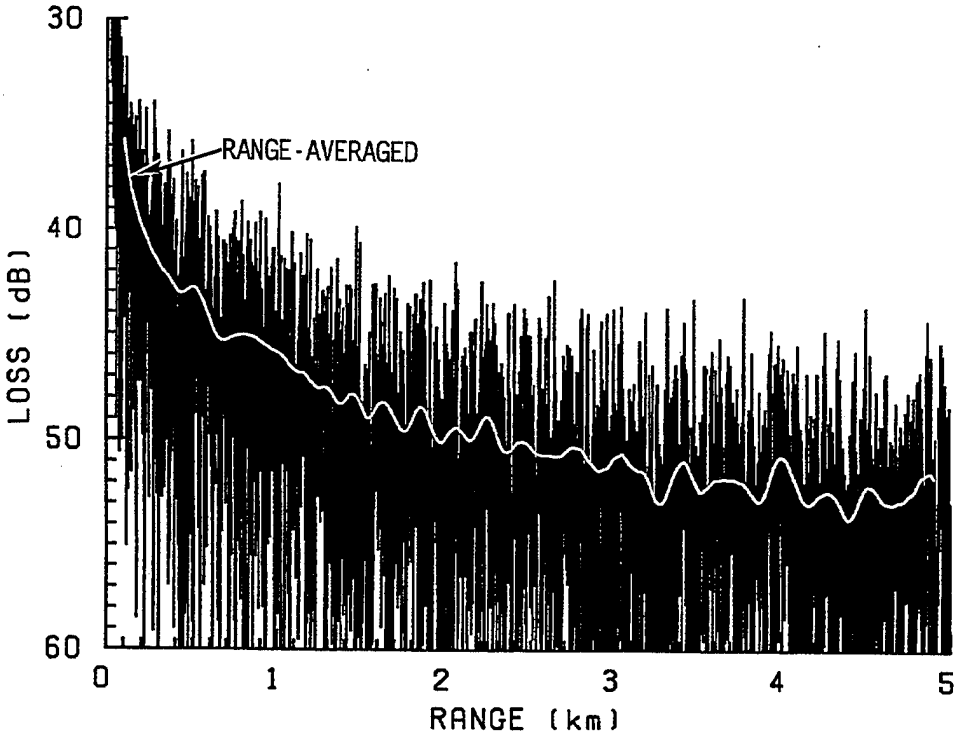

Figure 20. GRAB Random and Coherent Propagation Loss Predictions at 1 kHz for a Flat, Rocky Bottom

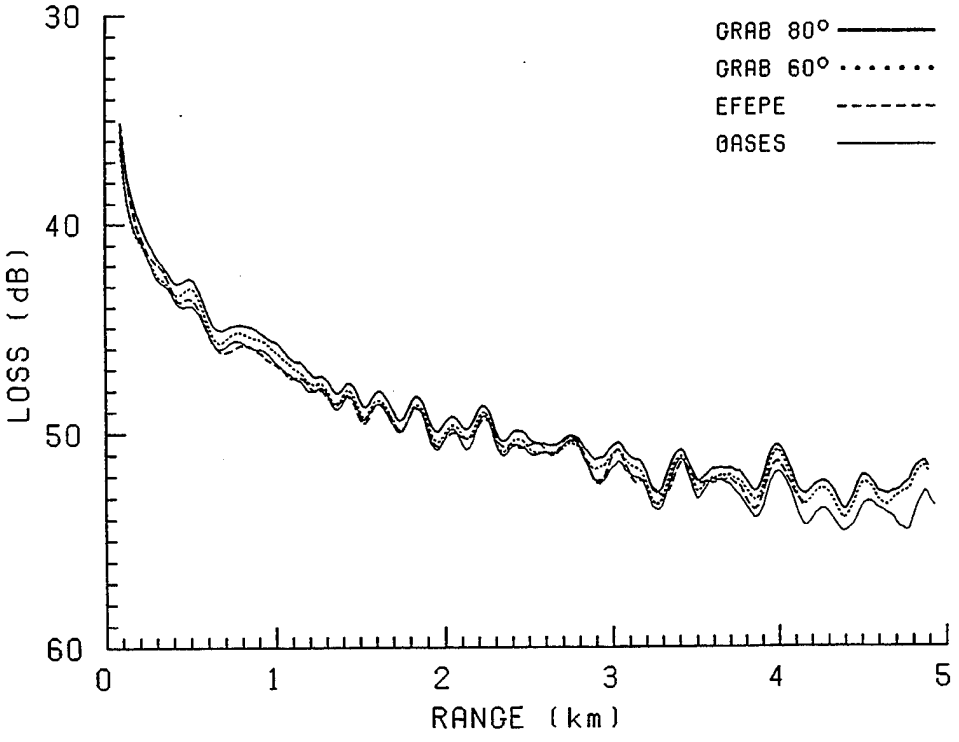

Figure 21. GRAB, EFEPE, and OASES Range-Averaged Propagation Loss Predictions at 1-kHz for a Flat, Rocky Bottom

3.2.3 Rock to Sand for Variable Bottom Depth

The actual scenario that prompted this series of tests was a downslope run where the bottom properties changed from rock to sand. Figure 16 shows that the slope redirects energy away from the surface duct. OASES is no longer applicable in this range-dependent environment, and GRAB must be baselined with EFEPE predictions.

First consider the effect of the slope with an all sand bottom. Figure 22 shows GRAB propagation loss contours for the flat 152.4 m and downslope bathymetries. As the ray trace figure 16 indicates, the overall levels at the 30.48-m receiver are lower when the bottom slopes downward.

Note that the coherent propagation losses at the 30.48-m receiver predicted by EFEPE and GRAB in figure 23 transition from rapid fluctuations over the rock bottom to slower fluctuations over sand. Little difference is seen in propagation loss levels over the rock (where the bottom is still relatively flat), but significant differences are seen between models over the sloping sand bottom at 2.315 km. Figure 24 compares 0.01852-m range-averaged EFEPE and GRAB predictions with the random phase GRAB prediction.

Figure 25 shows coherent and random GRAB predictions at 21 kHz without volume attenuation. The 1-kHz and 21-kHz predictions are similar because the bottom loss is nearly the same for the two frequencies, and neither has surface or volume losses. Thus, the comparison illustrates how energy is distributed in the water column. The higher interference rate at 21 kHz gives rise to rapid, coherent 15-dB fluctuations. In many applications the random addition provides a more robust measure of the propagation loss.

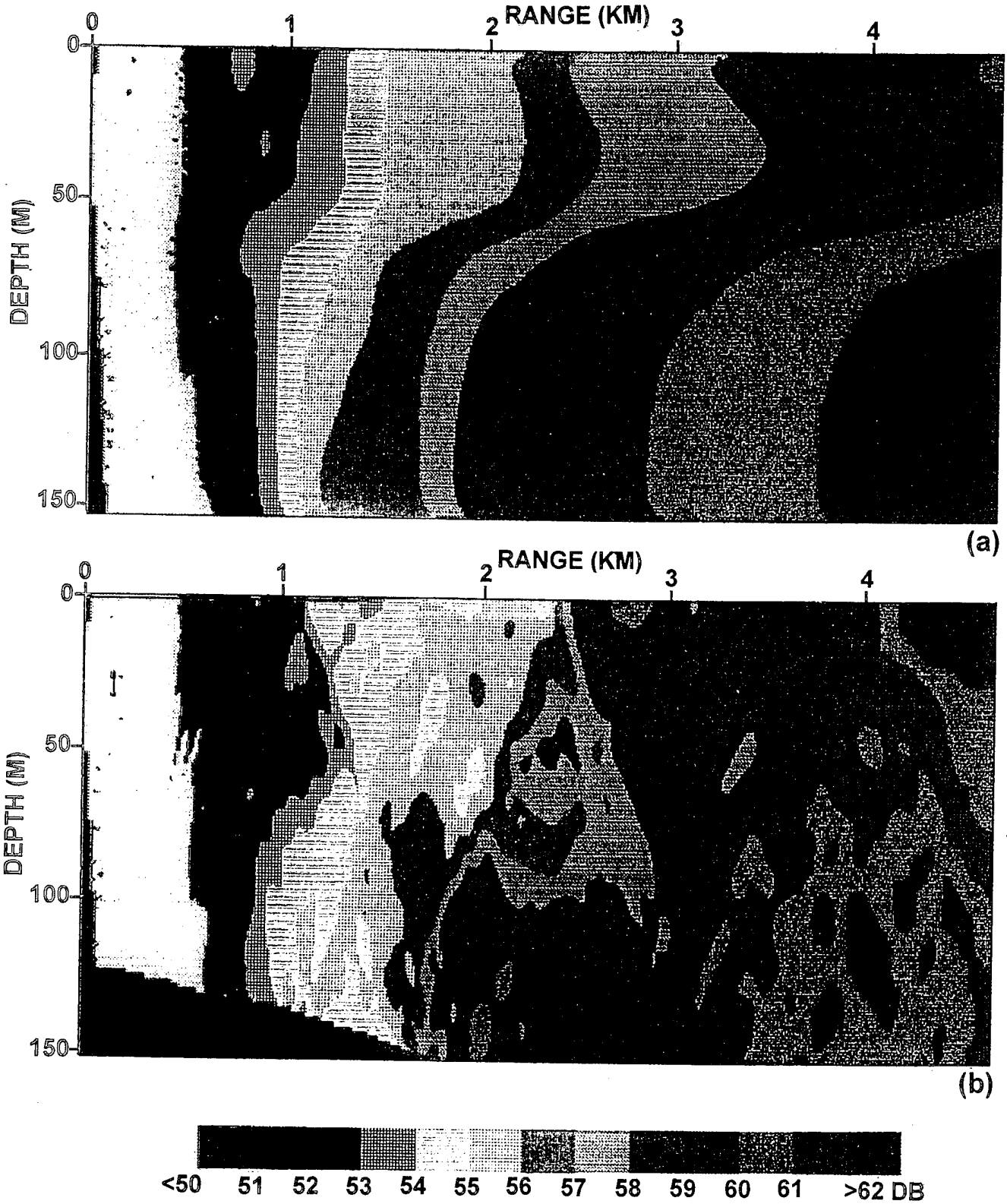

Figure 22. GRAB Propagation Loss Contours at 1 kHz for a Sandy Bottom: (a) Flat and (b) Downslope Bathymetry

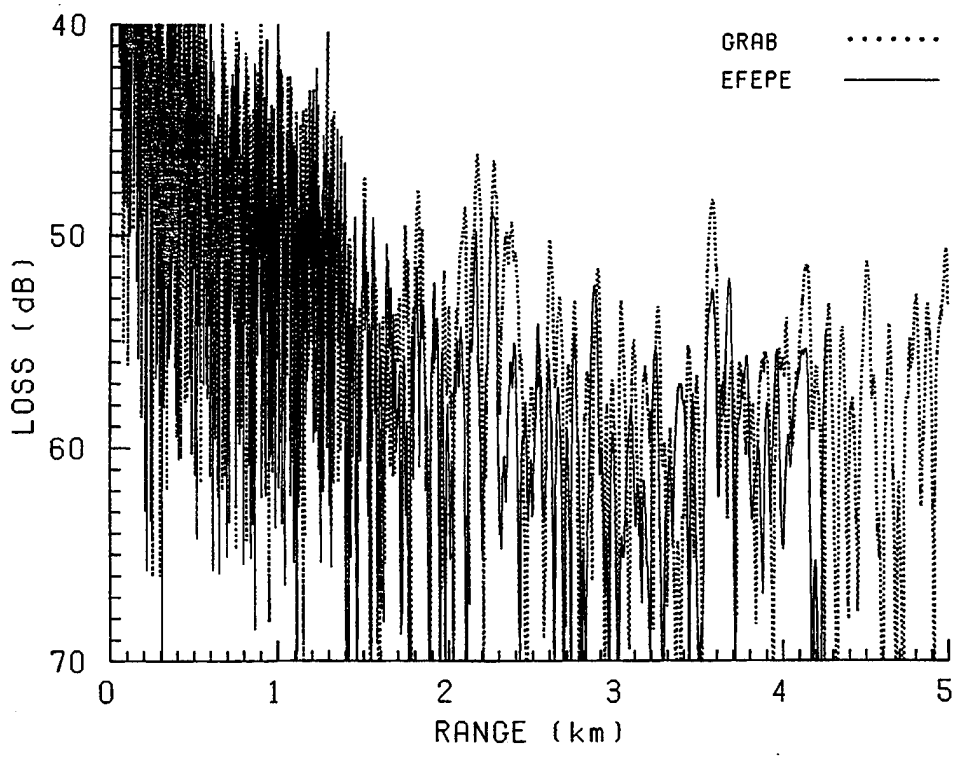

Figure 23. EFEPE and GRAB Propagation Loss Predictions at 1 kHz for a Rock-to-Sand Downslope Bathymetry

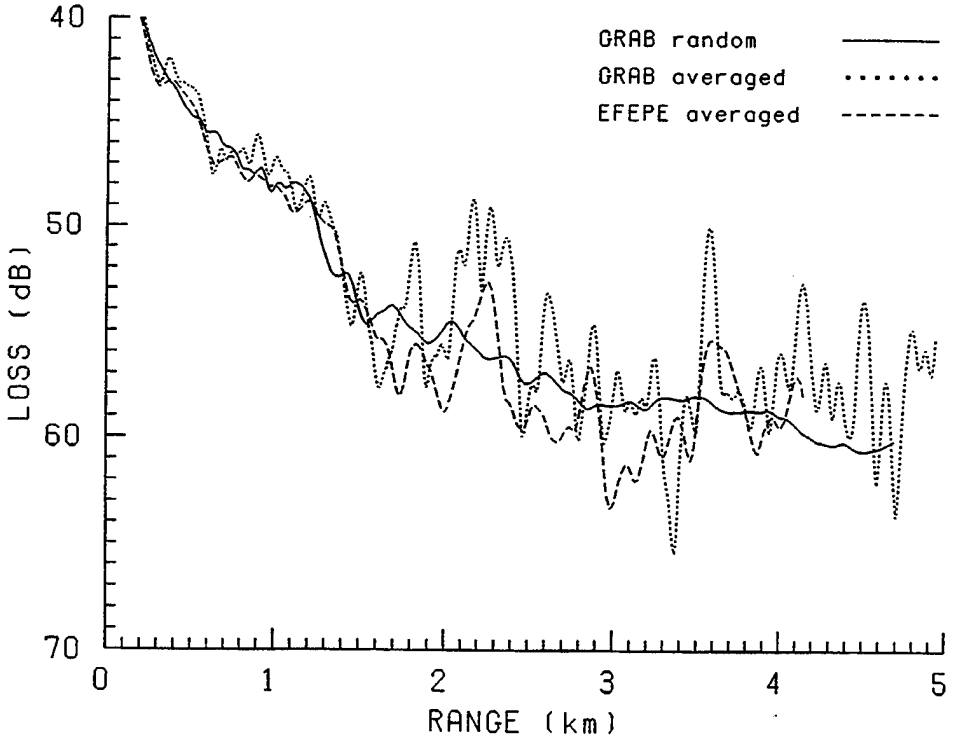

Figure 24. EFEPE and GRAB Range-Averaged Propagation Loss Predictions at 1 kHz for a Rock-to-Sand Downslope Bathymetry

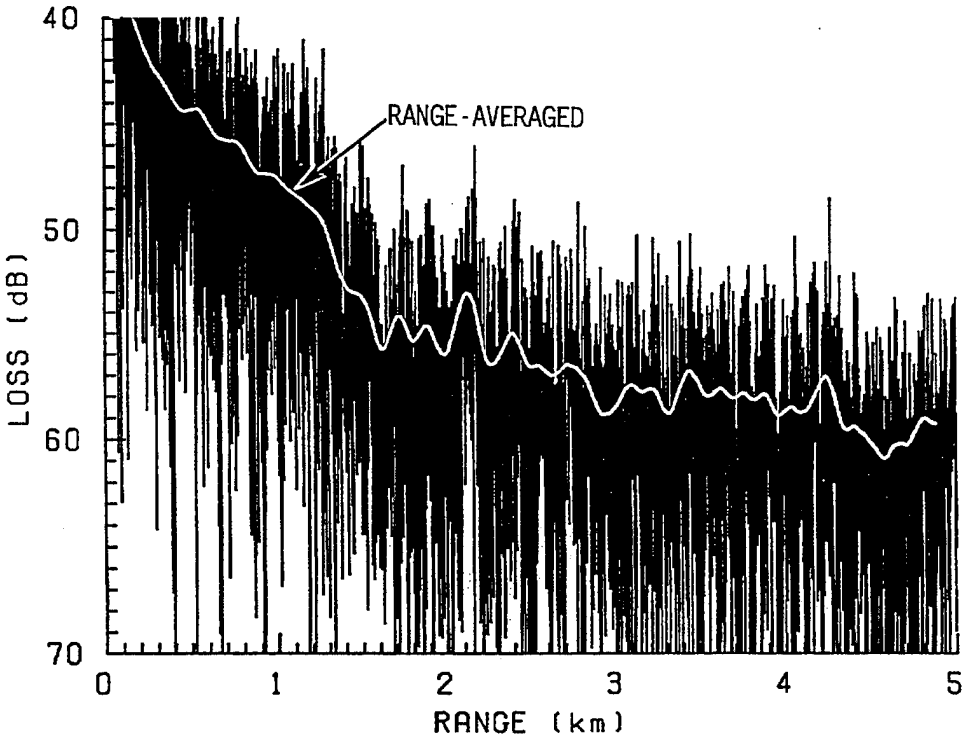

Figure 25. GRAB Propagation Loss Predictions at 21 kHz for a Rock-to-Sand Downslope Bathymetry

4. SUMMARY AND CONCLUSIONS

To summarize, a high-frequency propagation loss model was developed to investigate shallow ocean environments. The model is based on $N \times 2D$ ray tracing, Gaussian ray bundles, and virtual rays. The ray tracing determines ray trajectories, inclination angles and losses due to volume attenuation, and the ocean boundaries along numerous test rays. The Gaussian ray bundles replace the classical spreading loss of geometrical acoustics. The area under a ray bundle is chosen to conserve energy, while the algorithm for its standard deviation was derived by fitting results at a smooth caustic. Contributions from the tails of bundles that extend into the ocean boundaries are recovered by unfolding test rays into virtual rays at the appropriate boundary.

Ray bundles that undergo the same number of surface and bottom reflections are combined into acoustic eigenrays. An eigenray amplitude is simply the power sum of its ray bundles. Weighted sums yield the remaining parameters. The random addition propagation loss at a field point is the power addition of all eigenrays to the point and equals the power addition of the contributing ray bundles. However, the coherent addition propagation loss is the coherent addition of all eigenrays and generally does not equal the coherent addition of the ray bundles.

Although rigorous justification is not currently available, the Gaussian ray bundle method appears to be valid over a larger band of frequencies than originally intended. Its applicability is being established by comparison with various Navy "standards" and at-sea measurements. Results for the classic convergence zone and shallow-water test cases are encouraging.

Future plans include resolving some of the more questionable aspects of the model. In addition to the lack of mathematical rigor, phase errors occur at turning points and caustics. As with many ray-tracing models, the selection of test rays is left to the user. Too few may jeopardize fidelity; too many may be costly. Current experience calls for vertical angle increments of 0.1 to 0.01°. Away from caustics, real eigenrays are not sensitive to the lower bound of the ray bundle standard deviation. Since imaginary eigenrays are formed by the tails of Gaussian bundles, and these tails depend on the standard deviation, one should expect shadow zone propagation to be very sensitive to the lower bound. It is not known why the expression for the lower bound is so robust.

REFERENCES

1. D. Ludwig, "Uniform Asymptotic Expansions at a Caustic," *Communications on Pure and Applied Mathematics*, vol. XIX, pp. 215-250 (1966).

2. V. Cervený and J. E. P. Soares, "Fresnel Volume Ray Tracing," *Geophysics*, vol. 57, no. 7 (1992).

3. M. B. Porter and H. P. Bucker, "Gaussian Beam Tracing for Computing Ocean Acoustic Fields," *Journal of the Acoustical Society of America*, vol. 82, no. 4 (1987).

4. M. G. Brown, "A Maslov-Chapman Wavefield Representation for Wide-Angle One-Way Propagation," *Geophysics Journal International*, vol. 116, pp. 513-526 (1994).

5. H. Davis, H. Fleming, W. A. Hardy, R. Miningham, and S. Rosenbaum, "The Hudson Laboratories Ray Tracing Program," Technical Report No. 150, Hudson Laboratories of Columbia University, Dobbs Ferry, NY (1968).

6. L. A. Gainey and E. S. Holmes, "Software Product Specification of the Parabolic Equation V3.4," OAML-SPS-22, Scientific Applications International Corporation, Mashpee, MA (1992).

7. D. White and R. Moore, "System Design Description for the ASTRAL Model," OAML-SDD-23, Scientific Applications International Corporation, Mashpee, MA (1991).

8. M. D. Collins, "A Split-Step Pade Solution for the Parabolic Equation Method," *Journal of the Acoustical Society of America*, vol. 93, pp. 1736-1742 (1993).

9. H. Schmidt, "OASES: Ocean Acoustic and Seismic Exploration Synthesis," Massachusetts Institute of Technology, Cambridge, MA (1990).

10. M. A. Pedersen and D. F. Gordon, "Normal-Mode and Ray Theory Applied to Underwater Acoustic Conditions of Extreme Downward Refraction," *Journal of the Acoustical Society of America*, vol. 51, no. 1, part 2 (1972).

11. R. H. Hardin and F.D. Tappert, "Applications of the Split-Step Fourier Method to the Numerical Solution of Nonlinear and Variable Coefficient Wave Equations," *SIAM Review*, vol. 15, p. 423 (1973).

12. M. D. Collins and E. K. Westwood, "A Higher Order Energy Conserving Parabolic Equation for Range Dependent Ocean Depth, Sound Speed, and Density," *Journal of the Acoustical Society of America*, vol. 89 (1991).

13. H. Schmidt, "SAFARI (Seismo-Acoustic Fast field Algorithm for Range Independent Environments): User's Guide," SACLANT ASW Research Centre, LaSpezia, Italy (1987).

14. E. Miller, G. Hebenstreit, and R. Keenan, "Sound Speed Interpolation Mechanisms for Range-Dependent Models," 94-1093, Scientific Applications International Corporation, Mashpee, MA (1994).

APPENDIX
RAY-TRACING EQUATIONS

Ray-tracing equations, a generalized form of Snell's Law, may be obtained from the equation of characteristics for partial differential equations. In rectangular (x, y, z) coordinates,

$$\frac{d}{ds}\left(p\frac{dx}{ds}\right)=\frac{\partial p}{\partial x},$$

$$\frac{d}{ds}\left(p\frac{dy}{ds}\right)=\frac{\partial p}{\partial y}, \tag{A-1}$$

$$\frac{d}{ds}\left(p\frac{dz}{ds}\right)=\frac{\partial p}{\partial z},$$

where

$$ds=\sqrt{(dx)^2+(dy)^2+(dz)^2} \tag{A-2}$$

is the differential arc length along a ray path and the sound slowness $p = c^{-1}$ is the reciprocal of sound speed c. By confining the rays to the vertical plane $y = 0$ and setting the horizontal range $x = r$, equations (A-1) reduce to

$$\frac{d}{ds}\left(p\frac{dr}{ds}\right)=\frac{\partial p}{\partial r},$$

(A-3)

$$\frac{d}{ds}\left(p\frac{dz}{ds}\right)=\frac{\partial p}{\partial z}.$$

Multiplying these equations by p and applying the chain rule of ordinary differential equations yields

$$p\frac{dr}{ds}\frac{d}{dr}\left(p\frac{dr}{ds}\right)=p\frac{\partial p}{\partial r},$$

(A-4)

$$p\frac{dz}{ds}\frac{d}{dz}\left(p\frac{dz}{ds}\right)=p\frac{\partial p}{\partial z},$$

or, equivalently,

$$\frac{d}{dr}\left(p\frac{dr}{ds}\right)^2 = \frac{\partial p^2}{\partial r},$$

$$\frac{d}{dz}\left(p\frac{dz}{ds}\right)^2 = \frac{\partial p^2}{\partial z}. \tag{A-5}$$

In practice, equations (A-5) require numerical integration. Two general approaches are in use. The first assumes that the sound speed is a given function of position and approximates ray paths by evaluating standard integration formulas. The second approach approximates the sound speed in sectors so that equations (A-5) can be evaluated in closed form. The former approach tends to be more efficient if the integration step size is smaller than the distance across sectors. However, because it is difficult to estimate a suitable step size for the realistic conditions investigated here, the latter approach was selected instead. To be specific, the r - z plane is divided into triangular sectors, in each of which the gradient of slowness squared is

$$\nabla p^2 = \left(\frac{\partial p^2}{\partial r}, \frac{\partial p^2}{\partial z}\right) \equiv \text{constant}. \tag{A-6}$$

It should be noted that the ocean sound speed depends on temperature, salinity, and pressure. Since the variations of temperature and salinity are small in deep isothermal layers, the dependence of sound speed will be nearly linear with depth because of the increase of pressure with depth. In this case, it may be more efficient to approximate the sound speed in sectors in which the sound speed gradient rather than ∇p^2 is constant. The approach selected here offers certain numerical advantages in shallow water, such as working with parabolic ray segments instead of circular arcs.

Given equation (A-6), one can integrate equations (A-5) by rotating the coordinate system so that one component of ∇p^2 vanishes. The implementation used here integrates equations (A-5) directly to

$$\left(p\frac{dr}{ds}\right)^2 = \left(p\frac{dr}{ds}\right)_c^2 + (r - r_c)\frac{\partial p^2}{\partial r},$$

$$\left(p\frac{dz}{ds}\right)^2 = \left(p\frac{dz}{ds}\right)_c^2 + (z - z_c)\frac{\partial p^2}{\partial z}, \tag{A-7}$$

where the subscript $(\,)_c$ refers to values at the given point (r_c, z_c). Upon taking square roots, one obtains

$$\left(p\frac{dr}{ds}\right)=\sqrt{\left(p\frac{dr}{ds}\right)_c^2+(r-r_c)\frac{\partial p^2}{\partial r}},$$

$$\left(p\frac{dz}{ds}\right)=\pm\sqrt{\left(p\frac{dz}{ds}\right)_c^2+(z-z_c)\frac{\partial p^2}{\partial z}}, \tag{A-8}$$

for the horizontal and vertical components of slowness along the ray segment. It has been assumed that the range is strictly increasing. Also, the ± sign must be chosen so that $p\,dz/ds$ agrees with the vertical direction of the ray segment. Reversals in direction will be discussed shortly; for the time being, assume that there is no reversal in range or depth. Then, eliminating p/ds from equations (A-8) yields

$$\frac{dr}{\sqrt{\left(p\frac{dr}{ds}\right)_c^2+(r-r_c)\frac{\partial p^2}{\partial r}}}=\pm\frac{dz}{\sqrt{\left(p\frac{dz}{ds}\right)_c^2+(z-z_c)\frac{\partial p^2}{\partial z}}}. \tag{A-9}$$

Since the left-hand side of equation (A-9) depends explicitly on range, while the right-hand side depends explicitly on depth (range and depth are related implicitly by the ray path), equation (A-9) may be integrated from (r_c, z_c) to (r_d, z_d) to yield

$$2\left(\frac{\partial p^2}{\partial r}\right)^{-1}\left[\left(p\frac{dr}{ds}\right)_d-\left(p\frac{dr}{ds}\right)_c\right]=\pm2\left(\frac{\partial p^2}{\partial z}\right)^{-1}\left[\left(p\frac{dz}{ds}\right)_d-\left(p\frac{dz}{ds}\right)_c\right]. \tag{A-10}$$

Rationalizing the numerators of equation (A-10) and dividing by 2 gives

$$\Delta r\left[\left(p\frac{dr}{ds}\right)_c+\left(p\frac{dr}{ds}\right)_d\right]^{-1}=\Delta z\left[\left(p\frac{dz}{ds}\right)_c+\left(p\frac{dz}{ds}\right)_d\right]^{-1}=\Delta h, \tag{A-11}$$

where

$$\Delta r=r_d-r_c,$$

$$\Delta z=z_d-z_c, \tag{A-12}$$

and Δh is introduced for convenience. Note that the ± sign has been removed by the rationalization process.

Two final auxiliary formulas are required. Setting (r, z) to (r_d, z_d) in equations (A-7) and using the differences of two squares, it is seen that

$$\left(p\frac{dr}{ds}\right)_d = \left(p\frac{dr}{ds}\right)_c + \Delta h\frac{\partial p^2}{\partial r},$$

$$\left(p\frac{dz}{ds}\right)_d = \left(p\frac{dz}{ds}\right)_c + \Delta h\frac{\partial p^2}{\partial z}. \qquad \text{(A-13)}$$

Now, suppose that r_d is given but z_d is currently unknown. Then, $(p\,dr/ds)_d$ can be found from the first of equations (A-8), and Δh can be found from the left-hand side of equation (A-11). Given Δh, $(p\,dz/ds)_d$ can be obtained readily from the second of equations (A-13). This allows solution of equation (A-11) for

$$\Delta z = \Delta h\left[\left(p\frac{dz}{ds}\right)_c + \left(p\frac{dz}{ds}\right)_d\right]. \qquad \text{(A-14)}$$

Similarly, if z_d is given but r_d is unknown, $(p\,dz/ds)_d$ can be found from the second of equations (A-8), and Δh can be found from the middle term of equation (A-11). Given Δh,$(p\,dr/ds)_d$ can be obtained readily from the first of equations (A-13), and equation (A-11) yields

$$\Delta r = \Delta h\left[\left(p\frac{dr}{ds}\right)_c + \left(p\frac{dr}{ds}\right)_d\right]. \qquad \text{(A-15)}$$

This completes the case in which there is no reversal in direction. Now suppose that

$$\left(p\frac{dz}{ds}\right)_c^2 > 0, \qquad \text{(A-16)}$$

but

$$(z - z_c)\frac{\partial p^2}{\partial z} < 0. \qquad \text{(A-17)}$$

To prevent the physically impossible

$$\left(p\frac{dz}{ds}\right)_d^2 < 0, \qquad \text{(A-18)}$$

the ray segment is terminated at the vertex depth z_d where

$$\left(p\frac{dz}{ds}\right)_d^2 = \left(p\frac{dz}{ds}\right)_c^2 + (z_d - z_c)\frac{\partial p^2}{\partial z} = 0. \tag{A-19}$$

That is, the ray is horizontal at (r_d, z_d). In the next case to be considered, the ray originates at a vertexing depth. Here, the vertical direction must be chosen so that

$$(z - z_c)\frac{\partial p^2}{\partial z} > 0. \tag{A-20}$$

Finally, if both $(p\,dz/ds)_c$ and $\partial p^2/\partial z$ vanish, the ray is a horizontal segment.

INITIAL DISTRIBUTION LIST

Addressee	No. of Copies
Commander, Submarine Force Atlantic	2
Commander, Submarine Force Pacific	2
Commander, Submarine Development Squadron 12	2
Defense Technical Information Center	12
Chief of Naval Research (ONR-321—J. Simmen (4), ONR-322—E. Chaiha (4), ONR-332—J. Bergin (3), ONR-333—K. Ng (3))	14
Chief of Naval Operations (Code N096)	2
Naval Research Laboratory (Attn: Technical Library)	3
Center for Naval Analyses	1
Naval Oceanographic Office	1
Fleet Numerical Meterology and Oceanography Center	3
Naval Postgraduate School (Attn: Technical Library)	2
Naval War College (Attn: Technical Library)	2
Naval Sea Systems Command (SEA-91 (2), SEA-92 (2), PMO-425 (2), PEO-MIW (2), ASTO-E—P. Tiedeman (3), PMO-402 (3), PMO-403 (3), PMO-406 (3), PMO-411, PMO-415 (3), PMO-427 (3))	27
Naval Undersea Warfare Center Division, Keyport, WA	1
Naval Surface Warfare Center Coastal Systems Station	2
Naval Air Warfare Center	2
Scientific Applications International Corporation (Attn: R. Keenan) (Contract N66604-91-D-0613)	3
Applied Physics Laboratory, University of Washington (Contract N00039-91-C-0072)	3
Woods Hole Oceanographic Institution (Attn: K. Stewart) (Contract 1000014-94-0437)	1